Supplementary Materials for "Symmetry-engineered and electrically tunable in-plane anomalous Hall effect in oxide heterostructures"

Kunjie Dai[1,6], Zhen Wang[2,6], Wenfeng Wu[3,4,6], Feng Jin[1], Enda Hua[1], Nan Liu[4], Jingdi Lu[1], Jinfeng Zhang[1], Yuyue Zhao[1], Linda Yang[1], Kai Liu[1], Huan Ye[1], Qiming Lv[1], Zhengguo Liang[1], Ao Wang[1], Dazhi Hou[1,2], Yang Gao[2], Jing Tao[2], Liang Si[4] *, Wenbin Wu[1,5]*, and Lingfei Wang[1]*

[1] Hefei National Research Center for Physical Sciences at the Microscale, University of Science and Technology of China, Hefei 230026, China.

[2] Department of Physics, University of Science and Technology of China, Hefei 230026, China.

[3] Key Laboratory of Materials Physics, Institute of Solid State Physics, HFIPS, Chinese Academy of Sciences, Hefei 230031, China.

[4] School of Physics, Northwest University, Xi'an 710127, China.

[5] Anhui Key Laboratory of Condensed Matter Physics at Extreme Conditions, High Magnetic Field Laboratory, Chinese Academy of Sciences, Hefei 230031, China.

[6] These authors contribute equally to this work: Kunjie Dai, Zhen Wang, Wenfeng Wu.

* Corresponding author. Email: wanglf@ustc.edu.cn, wuwb@ustc.edu.cn, siliang@nwu.edu.cn.

Section 1: Epitaxial growth and physical properties of CRO/LCMO/CRO/NGO(110)$_O$ trilayer heterostructures

Section 2: Structural symmetry analyses of CRO/LCMO/CRO/NGO(110)$_O$ trilayer heterostructures based on XRD

Section 3: STEM characterizations of CRO/LCMO/CRO/NGO(110)$_O$ trilayers

Section 4: Additional IP-AHE measurements of CRO/LCMO/CRO/NGO(110)$_O$ trilayers

Section 5: Additional DFT calculation results

Section 6: Supporting results and DFT calculations related to ionic liquid gating of IP-AHE

Section 1. Epitaxial growth and physical properties of CRO/LCMO/CRO/NGO $(110)_O$ trilayer heterostructures.

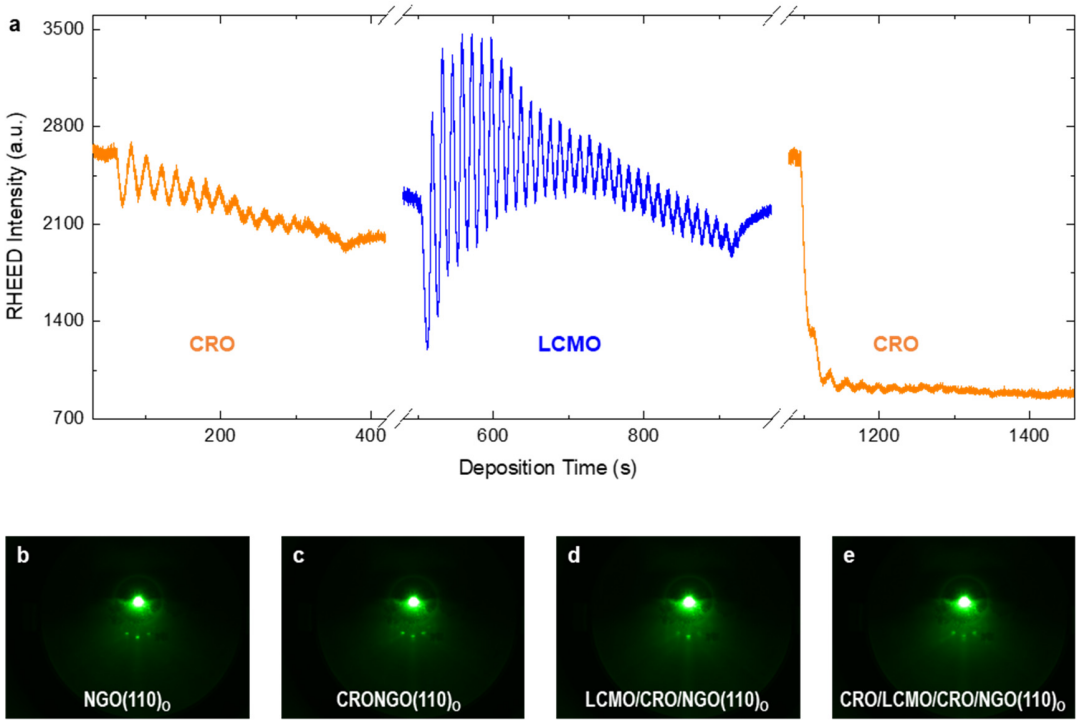

Supplementary Fig. 1 | RHEED monitoring of CRO and LCMO thin film deposition.
(**a**) Time-dependent reflection high-energy electron diffraction **(**RHEED) intensity profile recorded during pulsed laser deposition (PLD) of three subsequent layers: 16 unit-cells (u.c.) $CaRuO_3$ (CRO), 32 u.c. $La_{2/3}Ca_{1/3}MnO_3$ (LCMO), and subsequent 16 u.c. CRO. The clear oscillations of RHEED intensities suggest that both the CRO and LCMO layers are grown in a typical layer-by-layer mode. (**b-e**) RHEED diffraction patterns extracted from the bare $NdGaO_3(110)_O$ [$NGO(110)_O$] substrate surface (b), $CRO/NGO(110)_O$ thin film surface (c), $LCMO/CRO/NGO(110)_O$ bilayer surface (d), and $CRO/LCMO/CRO/NGO(110)_O$ trilayer surface (e).

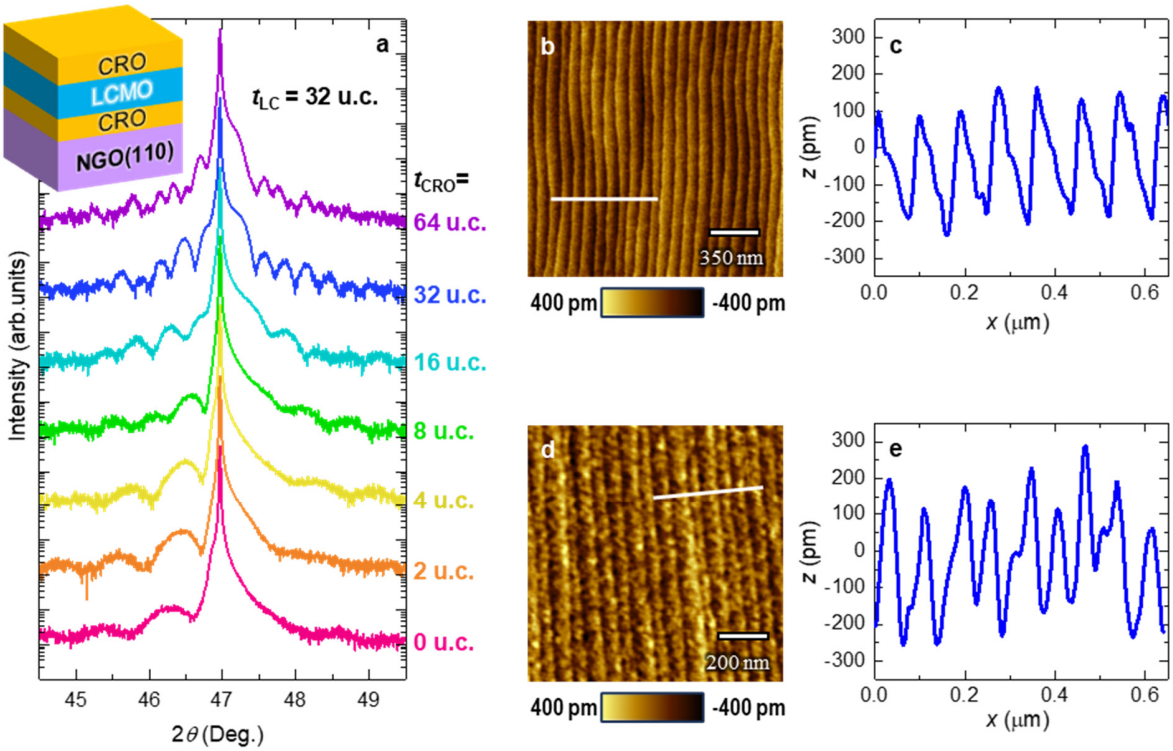

Supplementary Fig. 2 | XRD and AFM characterizations of CRO/LCMO/CRO trilayer heterostructures.

(**a**) X-ray diffraction (XRD) 2θ-ω linear scans measured from CRO/LCMO/CRO/NGO(110)$_O$ trilayer heterostructures with fixed LCMO layer thickness (t_{LC} = 32 u.c.) and various CRO layer thicknesses (t_{CRO}, from 0 to 32 u.c.). These XRD 2θ-ω linear scans display well-defined Laue fringes, signifying sharp heterointerfaces and high epitaxial quality. (**b,c**) Atomic force microscopy (AFM) image (b) and corresponding line profile of z-height signal (c) measured from a thermally-annealed NGO(110)$_O$ substrate, which clearly signifies the existence of single-cell-height surface terraces. (**d,e**) AFM image and z-height line profile measured from a CRO(16 u.c.)/LCMO(32 u.c.)/CRO(16 u.c.)/NGO(110)$_O$ trilayer heterostructure. This AFM image also displays a terraced surface morphology, which further corroborates the high epitaxial quality.

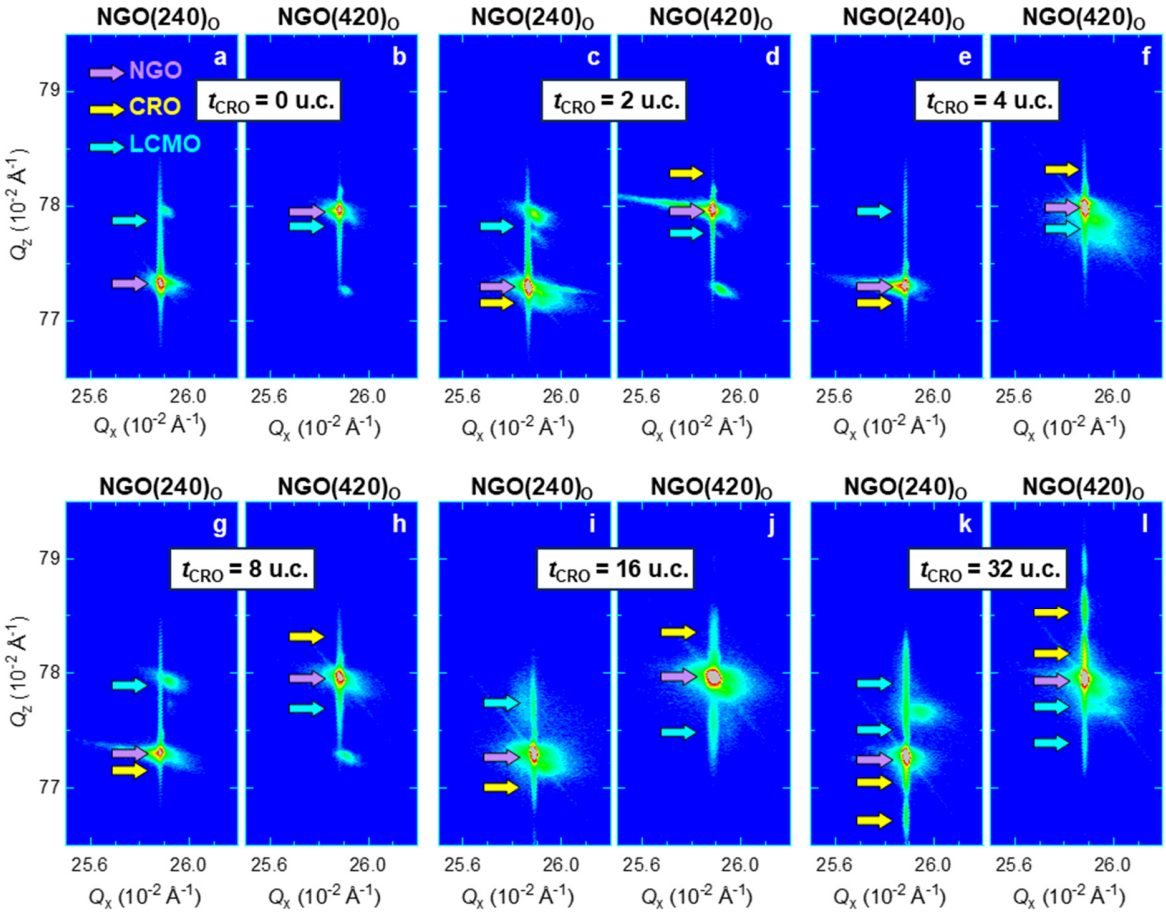

Supplementary Fig. 3 | RSM of CRO/LCMO/CRO trilayer heterostructures.

(**a-l**) Reciprocal space mappings (RSMs) measured from a series of CRO/LCMO(32 u.c.)/CRO/NGO(110)$_O$ trilayer heterostructures with various t_{CRO}. The diffraction spots from CRO, LCMO, and NGO are marked by solid arrows in yellow, blue, and purple, respectively. In all of the RSMs, the in-plane reciprocal space vectors (Q_x) of the films are the same as those of the substrate, demonstrating a coherent strain state.

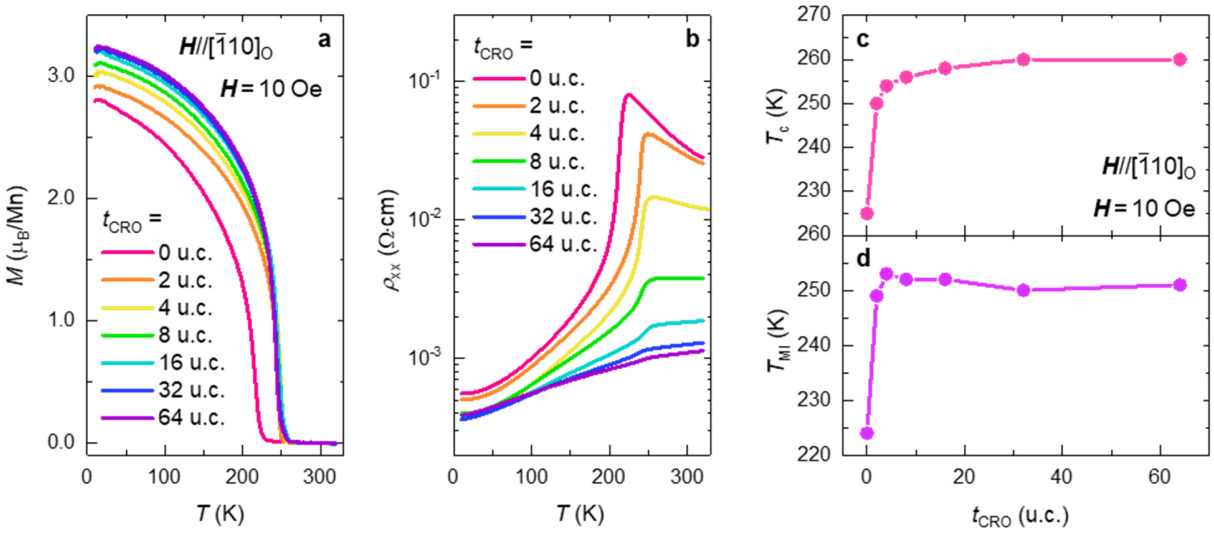

Supplementary Fig. 4 | Electrical transport and magnetic properties of CRO/LCMO/CRO trilayers. (**a,b**) Temperature-dependent magnetization (*M*-*T*) curves (a) and longitudinal resistivity (ρ_{xx}-*T*) curves (b) measured from a series of CRO/LCMO(32 u.c.)/CRO/NGO(110)$_O$ trilayer heterostructures with various t_{CRO}. These *M*-*T* and ρ_{xx}-*T* curves clearly display paramagnetic insulator-to-ferromagnetic metal (PMI-FMM) transitions, which are commonly observed in rare-earth doped manganites[1]. (**c,d**) Summary of t_{CRO}-dependent Curie temperature (T_C) curve (c) and insulator-to-metal transition temperature (T_{MI}) curve (d). As t_{CRO} increases from 0 to 2 u.c., the t_{CRO}-dependent T_C and T_{MI} increase sharply, which suggests that an ultrathin CRO layer can stabilize the FM phase in the LCMO layer through interfacial charge transfer[2-4].

Section 2. Structural symmetry analyses of CRO/LCMO/CRO/NGO(110)$_O$ trilayer heterostructures based on XRD

According to Supplementary Section 1, the XRD linear scans and RSMs have confirmed the high-epitaxial quality and coherent strain states of our CRO/LCMO/CRO/NGO(110)$_O$ trilayers. In this section, we further employ the RSM to analyze their structural symmetries.

We begin by explaining how to evaluate the orthorhombic symmetry of ABO_3 perovskite oxides from RSMs. Due to variations in the BO_6 oxygen octahedral rotation (OOR) patterns and deformation modes, the lattice constants of orthorhombic perovskites can exhibit two possible cases: $a_O > b_O$ or $a_O < b_O$. These two structural variation cases can be parameterized using the orthorhombicity $d_{OR} = 1 - a_O/b_O$. For most of the conventional orthorhombic perovskite oxides with $a^-a^-c^+$ type OOR pattern, such as CRO and NGO, $a_O < b_O$ and $d_{OR} > 0$. But for the orthorhombic perovskite oxides with considerable octahedral deformations, such as $SrRuO_3$ and LCMO, $a_O > b_O$ and $d_{OR} < 0$. For the $(110)_O$-oriented perovskite oxide heterostructures, the different d_{OR} of each constituent layer and substrate can be evaluated by the RSM. As schematically illustrated in Supplementary Fig. 5a, given a $(110)_O$-oriented perovskite oxide with $d_{OR} > 0$ ($a_O < b_O$, such as NGO and CRO), the interplanar d-spacing of the $(240)_O$ crystallographic plane is larger than that of the $(420)_O$ crystallographic plane. Consequently, the out-of-plane reciprocal space vector Q_z of $(420)_O$ diffraction is higher than that of $(240)_O$ diffraction (Supplementary Fig. 5b). On the contrary, given a $(110)_O$-oriented perovskite oxide with $d_{OR} < 0$ ($a_O > b_O$, such as LCMO), the interplanar d-spacing of the $(240)_O$ crystallographic plane is smaller than that of $(420)_O$ crystallographic plane (Supplementary Fig. 5c), thus making the Q_z of $(420)_O$ diffraction lower than that of $(240)_O$ diffraction (Supplementary Fig. 5d). By contrast, for both cases, the $(332)_O$, and $(33\bar{2})_O$ diffractions share the same Q_z value of $(330)_O$ diffraction, because the c_O axis is always perpendicular to the a_O and b_O axes. As the amplitude of d_{OR} (negative or positive) increases, the Q_z difference between $(420)_O$ and $(240)_O$ will also become larger, which makes the RSMs acquired near $(420)_O$ and $(240)_O$ diffractions a powerful tool for evaluating the symmetry of orthorhombic perovskites.

Now we turn to analyze the epitaxial relationships of our CRO/LCMO/CRO/NGO(110)$_O$ trilayer heterostructures. According to the RSM results shown in Figs. 2a-d and Supplementary Fig. 3, the reciprocal space positions $(420)_O$, $(240)_O$, $(332)_O$, and $(33\bar{2})_O$ diffractions of CRO, LCMO, and NGO are schematically illustrated in Supplementary Figs. 6a,b. For the $(420)_O$ diffractions, $Q_{z\text{-CRO}} > Q_{z\text{-NGO}} > Q_{z\text{-LCMO}}$, but for $(240)_O$ diffraction, $Q_{z\text{-LCMO}} > Q_{z\text{-NGO}} > Q_{z\text{-CRO}}$. Based on these results and the above discussions on the different d_{OR} for LCMO, NGO, and CRO (Supplementary Fig. 6c), we conclude that our CRO/LCMO/CRO/NGO(110)$_O$ heterostructure grows in an axis-to-axis epitaxial relationship: CRO$[100]_O$//LCMO$[100]_O$//NGO$[100]_O$ and CRO$[010]_O$//LCMO$[010]_O$//NGO$[010]_O$ (Supplementary Fig. 6d). This unique epitaxial relationship, driven by the interfacial connectivity of BO_6 octahedra, has been widely observed in orthorhombic perovskite oxide heterostructures[5-10].

Based on the RSM revealed epitaxial relationship of our CRO/LCMO/CRO/NGO(110)$_O$ trilayers, we now analyze the detailed structural symmetry breaking in the LCMO layer, which is closely coupled with the in-plane anomalous Hall effect (IP-AHE). In bulk, LCMO adopts the orthorhombic space group *Pbnm*, and the corresponding symmetry operations are listed in Supplementary Table 1 and illustrated in Supplementary Fig. 7a. In brief, bulk LCMO possesses 3 twofold-rotation axes (along $[100]_O$, $[010]_O$, and $[001]_O$, denoted as $2_{[100]}$, $2_{[010]}$, and $2_{[001]}$) as well as 3 mirror planes [parallel to $(100)_O$, $(010)_O$, and $(001)_O$,

denoted $m_{(100)}$, $m_{(010)}$, and $m_{(001)}$]. However, in the CRO/LCMO/CRO trilayer heterostructures, these structural symmetry operations in the LCMO layer may vanish due to the interface-induced symmetry breaking. Specifically, the top and bottom CRO/LCMO heterointerfaces will eliminate two mirror planes [$m_{(010)}$ and $m_{(100)}$] and two secondary rotation axes ($2_{[100]}$ and $2_{[010]}$) (Supplementary Fig. 7b). As a result, the LCMO layer in the CRO/LCMO/CRO trilayer heterostructures has only one mirror plane [$m_{(001)}$] and one secondary rotation axis $2_{[001]}$, which leads to a symmetry lowering from orthorhombic (space group: *Pbnm*) to monoclinic (space group: $P2_1/m$, the corresponding point group is C_{2h}). This symmetry-lowering can be corroborated by the summary of symmetry operations of space group $P2_1/m$ in Supplementary Table 2.

The above symmetry lowering from orthorhombic *Pbnm* to monoclinic $P2_1/m$ can be visualized by converting the orthorhombic unit-cell into the pseudo-cubic unit-cell. The crystallographic indexes in orthorhombic and pseudo-cubic notations are denoted by subscript "O" and "p", respectively. The conversion from orthorhombic to pseudo-cubic unit-cell is illustrated in Supplementary Fig. 8a. The relationships between the orthorhombic and pseudo-cubic unit-cells are as follows:

$$a_\mathrm{p} = c_\mathrm{p} = \frac{1}{2}\sqrt{(a_\mathrm{O}^2 + b_\mathrm{O}^2)}\,, b_\mathrm{p} = \frac{c_\mathrm{O}}{2}$$

$$\alpha = 90°,\ \beta = 2\arctan\left(\frac{a_\mathrm{O}}{b_\mathrm{O}}\right),\ \gamma = 90°$$

When converting the orthorhombic unit-cell into the pseudo-cubic unit-cell, the unequal a_O and b_O deviate the β angle from 90°. As depicted in Supplementary Fig. 8b, the c_p axis tilts towards the a_p axes while remaining perpendicular to the b_p axis ($\alpha = 90°$ but $\beta \neq 90°$), yielding a monoclinic unit-cell (in other words, a monoclinic-like distortion). The angle β can be directly determined by the orthorhombicity ($d_\mathrm{O} = 1 - a_\mathrm{O}/b_\mathrm{O}$). For NGO and CRO unit-cells with $a_\mathrm{O} < b_\mathrm{O}$, $\beta_\mathrm{CR} < \beta_\mathrm{NGO} < 90°$, and for LCMO unit-cells with $a_\mathrm{O} > b_\mathrm{O}$, $\beta_\mathrm{LC} > 90°$ (as depicted in Fig. 2e and Supplementary Fig. 6d). According to the analyses shown in Supplementary Fig. 5, the layer-averaged β angles of CRO and LCMO layers can be easily derived from the RSM results (Supplementary Fig. 3) by the following equation:

$$\beta = 2\arctan\left(\frac{\Delta|Q_\mathrm{z}|}{2|Q_\mathrm{x}|}\right) \quad (1)$$

where $\Delta|Q_\mathrm{z}|$ is the Q_z difference between the $(420)_\mathrm{O}$ and $(240)_\mathrm{O}$ diffraction spots. Using this formula, we calculated the tilt angle β of the pseudo-cubic unit-cells of NGO substrate, CRO layer, and LCMO layers in the CRO/LCMO/CRO/NGO$(110)_\mathrm{O}$ trilayer heterostructures, as summarized in Supplementary Table 3.

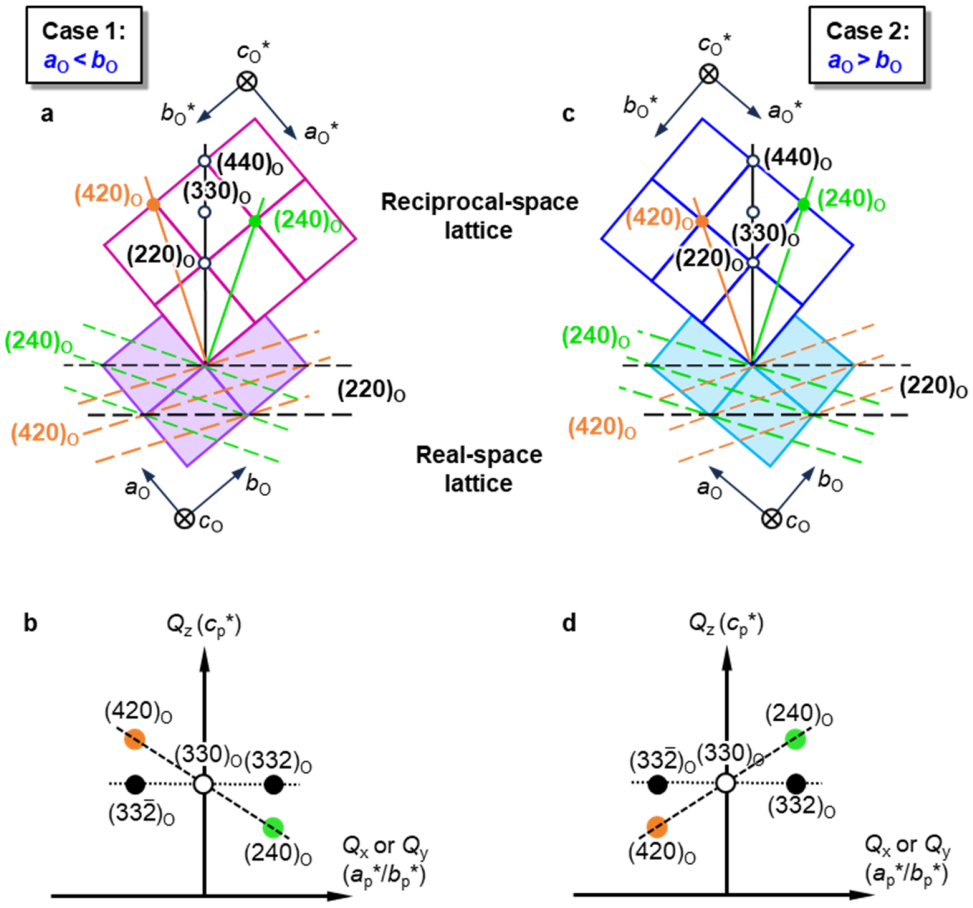

Supplementary Fig. 5 | Schematic illustration of the correlation between RSM and orthorhombicity.

(**a**,**c**) Transformation relationship between real space and reciprocal space for orthorhombic lattice with $d_{OR} > 0$ ($a_O < b_O$, such as NGO and CRO) (a) and $d_{OR} < 0$ ($a_O > b_O$, such as LCMO) (c). In the diagram, a_O, b_O, and c_O are the basis vectors of the real lattice space, and a_O*, b_O*, and c_O* are the basis vectors of the reciprocal lattice space. The black, orange, and green dashed lines correspond to the $(220)_O$, $(420)_O$, and $(240)_O$ crystal planes, respectively. Their corresponding reciprocal lattice points are shown as black open circles and orange and green solid circles, respectively. (**b,d**) Schematic illustration of diffraction spots corresponding to the reciprocal lattice with (b) $d_{OR} > 0$ (such as NGO and CRO) and (d) $d_{OR} < 0$ (such as LCMO). The horizontal axis represents the in-plane reciprocal vectors of the pseudo-cubic lattice, corresponding to (Q_x and Q_y) in the RSM, and the vertical axis represents the out-of-plane reciprocal representation of the pseudo-cubic lattice, corresponding to (Q_z) in the RSM.

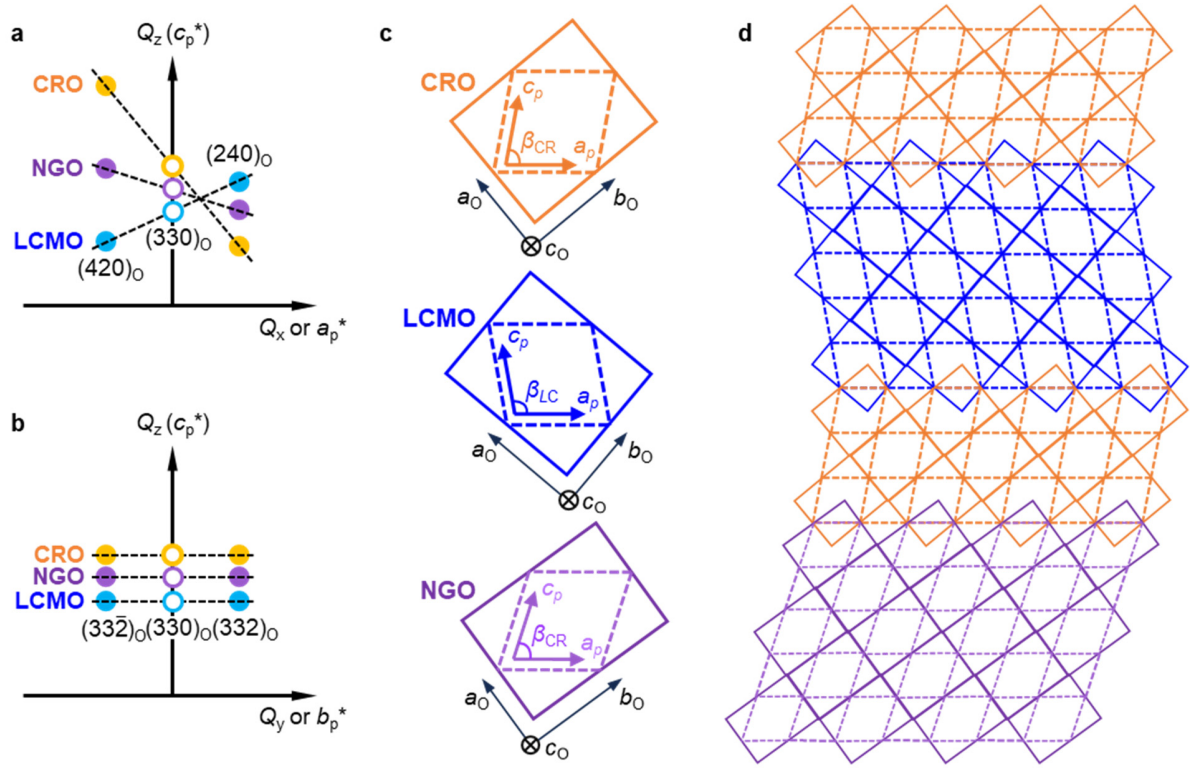

Supplementary Fig. 6 | Axis-to-axis growth of the CRO/LCMO/CRO/NGO(110)$_O$ trilayers. (**a**,**b**) A schematic diagram of the reciprocal space positions (420)$_O$, (240)$_O$, (332)$_O$, and (33$\bar{2}$)$_O$ diffractions of trilayer heterostructures. The horizontal axis is the pseudo-cube a_p*-axis (a), corresponding to Q_x of the RSM, and the vertical axis is the pseudo-cube c_p*-axis, corresponding to Q_z of the RSM; the horizontal axis is the pseudo-cube b_p*-axis (b), corresponding to Q_y of the RSM, and the vertical axis is the pseudo-cube c_p*-axis, corresponding to Q_z of the RSM; the blue, purple, and yellow solid dots correspond to the reciprocal lattice points of LCMO, NGO, and CRO, respectively. (**c**) Schematic diagram of cross sections of orthorhombic unit-cell (solid lines) and pseudo-cubic unit-cell (dashed lines) of CRO (yellow), LCMO (blue), and NGO (purple) perpendicular to the c_O-axis. The angle between a_p and c_p in the pseudo-cubic unit-cell is β. (**d**) The epitaxial relationship of the CRO/LCMO/CRO trilayer heterostructures grown on NGO(110)$_O$. The orthorhombic unit-cells are plotted by solid rectangles, and the pseudo-cubic unit-cells are plotted by dashed rhombuses.

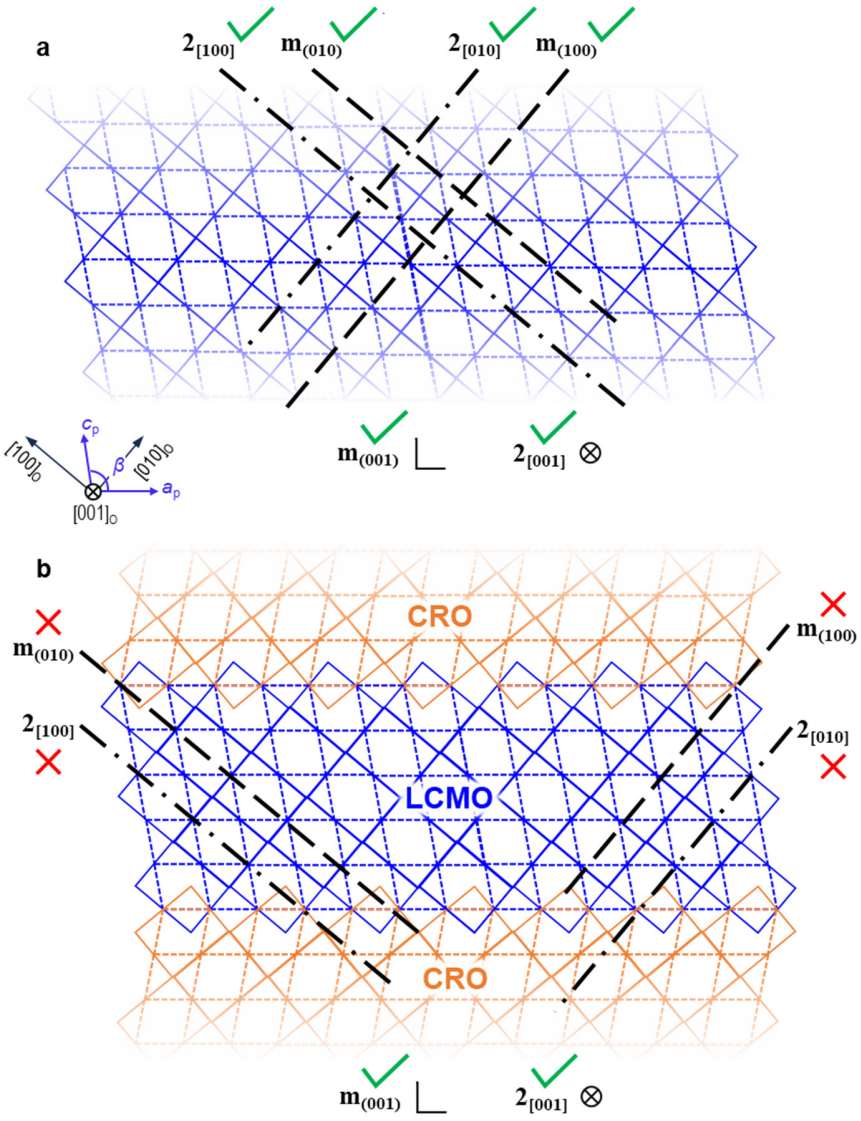

Supplementary Fig. 7 | Symmetry lowering of the LCMO layer in the CRO/LCMO/CRO/NGO(110)$_O$ trilayer heterostructures.

(**a**) Schematic diagram of the symmetry operations in LCMO bulk. (**b**) Symmetry operations that are eliminated/preserved in heterostructures due to the presence of heterointerfaces. The orthorhombic unit-cells are plotted by solid rectangles, and the pseudo-cubic unit-cells are plotted by dashed rhombuses. The 2-fold rotation axes are marked by the thick, dotted dashed lines and the "⊗" mark. The mirror planes are marked by thick, dashed lines and the "L" mark. The existence and absence of these symmetry operations are indicated by the "✓" and "×" marks, respectively.

No.	(x,y,z) form	Matrix form	Symmetry operation	
			ITA	Seitz
1	x, y, z	$\begin{pmatrix} 1 & 0 & 0 & 0 \\ 0 & 1 & 0 & 0 \\ 0 & 0 & 1 & 0 \end{pmatrix}$	1	{1|0}
2	$-x+1/2, -y, z+1/2$	$\begin{pmatrix} -1 & 0 & 0 & 1/2 \\ 0 & -1 & 0 & 0 \\ 0 & 0 & 1 & 1/2 \end{pmatrix}$	2 (0,0,1/2) 1/4,0, z	$\{2_{001} \mid 1/2\ 0\ 1/2\}$
3	$-x, y+1/2, -z$	$\begin{pmatrix} -1 & 0 & 0 & 0 \\ 0 & 1 & 0 & 1/2 \\ 0 & 0 & -1 & 0 \end{pmatrix}$	2 (0,1/2,0) 0, y,0	$\{2_{010} \mid 0\ 1/2\ 0\}$
4	$x+1/2, -y+1/2, -z+1/2$	$\begin{pmatrix} 1 & 0 & 0 & 1/2 \\ 0 & -1 & 0 & 1/2 \\ 0 & 0 & -1 & 1/2 \end{pmatrix}$	$2(1/2,0,0) \times 1/4,1/4$	$\{2_{100} \mid 1/2\ 1/2\ 1/2\}$
5	$-x, -y, -z$	$\begin{pmatrix} -1 & 0 & 0 & 0 \\ 0 & -1 & 0 & 0 \\ 0 & 0 & -1 & 0 \end{pmatrix}$	-1 0,0,0	{-1|0}
6	$x+1/2, y, -z+1/2$	$\begin{pmatrix} 1 & 0 & 0 & 1/2 \\ 0 & 1 & 0 & 0 \\ 0 & 0 & -1 & 1/2 \end{pmatrix}$	a x, y, 1/4	$\{m_{001} \mid 1/2\ 0\ 1/2\}$
7	$x, -y+1/2, z$	$\begin{pmatrix} 1 & 0 & 0 & 0 \\ 0 & -1 & 0 & 1/2 \\ 0 & 0 & 1 & 0 \end{pmatrix}$	m x, 1/4, z	$\{m_{010} \mid 0\ 1/2\ 0\}$
8	$-x+1/2, y+1/2, z+1/2$	$\begin{pmatrix} -1 & 0 & 0 & 1/2 \\ 0 & 1 & 0 & 1/2 \\ 0 & 0 & 1 & 1/2 \end{pmatrix}$	n (0,1/2,1/2) 1/4, y,z	$\{m_{100} \mid 1/2\ 1/2\ 1/2\}$

Supplementary Table 1 | Summary of symmetry operations in orthorhombic perovskite (space group: *Pbnm*).

For the orthorhombic perovskite (space group: *Pbnm*), there are eight symmetry operations in total. The first column lists the symmetry operation numbers; the second column (x,y,z) form shows the symmetry operations as coordinate transformations; the third Matrix form gives their matrix representations; the fourth ITA lists the International Tables for Crystallography (ITA) symbols; and the fifth Seitz symbols present their compact group-theoretical forms.

No.	(x,y,z) form	Matrix form	Symmetry operation	
			ITA	Seitz
1	x, y, z	$\begin{pmatrix} 1 & 0 & 0 & 0 \\ 0 & 1 & 0 & 0 \\ 0 & 0 & 1 & 0 \end{pmatrix}$	1	{1|0}
2	$-x, y+1/2, -z$	$\begin{pmatrix} -1 & 0 & 0 & 0 \\ 0 & 1 & 0 & 1/2 \\ 0 & 0 & -1 & 0 \end{pmatrix}$	2 (0,1/2,0) 0, y,0	$\{2_{010} \mid 0\ 1/2\ 0\}$
3	$-x, -y, -z$	$\begin{pmatrix} -1 & 0 & 0 & 0 \\ 0 & -1 & 0 & 0 \\ 0 & 0 & -1 & 0 \end{pmatrix}$	-1 0,0,0	{-1|0}
4	$x, -y+1/2, z$	$\begin{pmatrix} 1 & 0 & 0 & 0 \\ 0 & -1 & 0 & 1/2 \\ 0 & 0 & 1 & 0 \end{pmatrix}$	m x, 1/4, z	$\{m_{010} \mid 0\ 1/2\ 0\}$

Supplementary Table 2 | Summary of symmetry operations in monoclinic perovskite (space group: $P2_1/m$).

For the space group $P2_1/m$, there are four symmetry operations in total. The first column lists the symmetry operation numbers; the second column (x,y,z) form shows the symmetry operations as coordinate transformations; the third Matrix form gives their matrix representations; the fourth ITA lists the International Tables for Crystallography (ITA) symbols; and the fifth Seitz symbols present their compact group-theoretical forms.

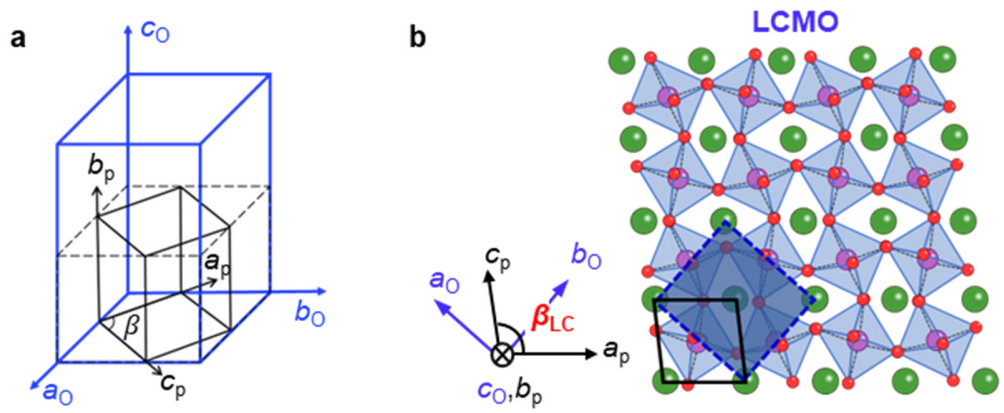

Supplementary Fig. 8 | Conversion from orthorhombic unit-cell to pseudo-cubic unit-cell.
(**a**) Conversion of orthorhombic unit-cell to pseudo-cubic unit-cell. (**b**) The schematic atomic structure of the LCMO unit-cell, viewed along the $[001]_O$ (in orthorhombic index) axis.

t_{CRO}	0 u.c.	2 u.c.	4 u.c.	8 u.c.	16 u.c.	32 u.c.	64 u.c.	Bulk
β_{CR}	–	88.82	88.74	88.70	88.47	88.75	88.69	87.99
β_{LC}	90.03	90.06	90.13	90.15	90.20	90.08	90.07	90.13
β_{NG}				89.26				89.26

Supplementary Table 3 | Summary of monoclinic tilting angle (β) in CRO/LCMO/CRO trilayers.
The β angles of CRO and LCMO layers (β_{CR} and β_{LC}, respectively) as well as the NGO substrate (β_{NG}) extracted from the diffraction spots in Supplementary Fig. 3 using Eq.1. The bulk values are calculated from the lattice constants reported in previous literature[11-13].

Section 3. STEM characterizations of CRO/LCMO/CRO/NGO(110)$_O$ trilayers

Based on the XRD analysis of structural symmetry in Supplementary Section 2, we now employ the scanning transmission electron microscopy (STEM) to characterize the structure of CRO/LCMO/CRO/NGO(110)$_O$ heterostructure at the atomic scale.

We first characterize the interfacial structure of CRO/LCMO/CRO/NGO(110)$_O$ trilayer heterostructure and LCMO/NGO(110)$_O$ thin film using STEM. As shown in Supplementary Fig. 9, the STEM images measured along [001]$_O$ zone-axis in high-angle annular dark-field (HAADF) mode confirm that all the CRO/LCMO and LCMO/NGO heterointerfaces are atomically sharp. The intermixing is highly confined within one interfacial unit-cell. In the CRO/LCMO/CRO stack, the bottom LCMO/CRO interface is terminated by RuO_2-(La,Ca)O configuration, while the top interface is terminated by the MnO_2-CaO configuration, which is a direct consequence of the layer-by-layer growth mode. This asymmetric interfacial termination configuration may further assist the interface-mediated symmetry-lowering discussed above.

Next, we utilize STEM-based geometric phase analysis (GPA) to further clarify the structural symmetry lowering and monoclinic-like distortion in the CRO/LCMO/CRO/NGO(110)$_O$ trilayer. The geometric phase $P_{\mathbf{g}}(\boldsymbol{r})$ can be extracted from STEM images (Supplementary Figs. 10a, d) using the following equation[14, 15]:

$$P_{\mathbf{g}}(\boldsymbol{r}) = -2\pi \mathbf{g} \cdot \boldsymbol{u}(\boldsymbol{r})$$

where $\boldsymbol{r} = (x, y)$ is the image coordinates, $\boldsymbol{g}$ is the reciprocal lattice vector, and $\boldsymbol{u}(\boldsymbol{r}) = (u_x, u_y)$ represents the local phase change caused by the displacement (i.e., the displacement field). For two non-collinear Bragg vectors $\boldsymbol{g_1}$ and $\boldsymbol{g_2}$, we obtain a system of linear equations:

$$\begin{bmatrix} u_x \\ u_y \end{bmatrix} = -\frac{1}{2\pi} \begin{bmatrix} g_{1x} & g_{1y} \\ g_{2x} & g_{2y} \end{bmatrix}^{-1} \begin{bmatrix} P_{g_1} \\ P_{g_2} \end{bmatrix}$$

The gradient of the displacement field gives the 2×2 strain tensor $E = \nabla \boldsymbol{u}$; It can be decomposed into a symmetric part (strain ε) and an antisymmetric part (rigid body rotation ω):

$$E = \begin{bmatrix} \partial u_x / \partial x & \partial u_x / \partial y \\ \partial u_y / \partial x & \partial u_y / \partial y \end{bmatrix}, \ \varepsilon = \frac{1}{2}(E + E^{\top}), \ \omega = \frac{1}{2}(E - E^{\top})$$

Here, the only independent component of ω is

$$\omega_{xy} = \frac{1}{2}\left(\frac{\partial u_y}{\partial x} - \frac{\partial u_x}{\partial y}\right)$$

It represents the local lattice rotation angle, which determines the cross-sectional tilting of unit-cells. In our case, the $\omega_{(100)_P}$ represents the local tilting of the $(100)_P$ plane [the $(\bar{1}10)_O$ plane in orthorhombic notation] in each pseudo-cubic unit-cell, and the $\omega_{(010)_P}$ represents the local tilting of $(010)_P$ plane [the $(001)_O$ plane in orthorhombic notation] in each pseudo-cubic unit-cell. The GPA analyses based on the STEM images of the CRO/LCMO/CRO/NGO(110)$_O$ trilayer (Supplementary Fig. 10a) and LCMO/NGO(110)$_O$ thin films (Supplementary Fig. 10d) are presented in Supplementary Figs. 10b, c and Supplementary Figs. 10e, f, respectively.

For the CRO/LCMO/CRO/NGO(110)$_O$ trilayer, the $\omega_{(100)p}$ contrasts for LCMO and CRO layers are homogeneous but show opposite signs (Supplementary Fig. 10b). Since the $\omega_{(100)p}$ value can represent the local β-90° value in each pseudo-cubic unit-cell, the STEM-GPA mappings reveal uniform monoclinic-like distortions in the CRO and LCMO layers, and the tilting directions are opposite. By contrast, the $\omega_{(010)p}$ contrasts are close to zero and nearly invisible (Supplementary Fig. 10c), suggesting a homogeneous local $\alpha = 0$. For the LCMO/NGO(110)$_O$ thin film, the $\omega_{(100)p}$ contrasts are much weaker, suggesting a decay of monoclinic-like distortion (Supplementary Figs. 10e, f). Based on these results, the STEM-GPA mappings clearly reveal CRO-enhanced monoclinic-like distortions on the unit-cell scale, which are consistent with the RSM results and analyses (Fig. 2 in the Main Text and Supplementary Section 2).

Now we turn to revealing the correlation between OOR and the monoclinic-like distortion in CRO/LCMO/CRO trilayer heterostructures via atomic-scale STEM images. According to Zayak et al.[16], the orthorhombic $a^-a^-c^+$-type OOR can be decomposed into the in-phase rotation along the [001]$_O$ axis and anti-phase tilting around the [010]$_O$ axis. The differences in a_O and b_O (i.e., the orthorhombicity $d_{OR} \neq 0$) are determined by the latter anti-phase tilting as well as octahedral deformations (i.e., Jahn-Teller distortion in MnO_6). On this basis, we acquired atomic-scale STEM images in both HAADF and annular bright-field (ABF) modes (Supplementary Figs. 11a, b) of the CRO/LCMO/CRO/NGO(110)$_O$ trilayer. From the STEM-HAADF image, we extracted the in-plane lattice constants for all of the LCMO and CRO atomic layers, which match perfectly with the atomic layers in the NGO(110)$_O$ substrate(Supplementary Fig. 11c), which further verified the coherent strain state of the trilayer heterostructure. In the STEM-ABF image, the observable oxygen contrast enables a direct determination of the in-plane B-O-B bond angle (η), which represents the degree of octahedral tilting. As shown in Supplementary Fig. 11d, the layer-resolved η values of NGO substrate, CRO, and LCMO layers are distinct from each other but continuously evolve at the heterointerfaces, which highlight the important role of interfacial octahedral connectivity. Moreover, the relative magnitudes of averaged η for NGO, CRO, and LCMO are $\eta_{CR} < \eta_{NG} < \eta_{LC}$, which is consistent with the relative magnitudes of monoclinic-like tilting angles ($\beta_{CR} < \beta_{NG} < \beta_{LC}$). Accordingly, the STEM-ABF images further verified that the monoclinic-like distortions in CRO/LCMO/CRO trilayer heterostructures originate from the combined effects of the heterointerface and the interfacial coupling of OOR.

We also acquire atomically-resolved STEM-HAADF and STEM-ABF images from the LCMO/NGO(110)$_O$ thin film (Supplementary Figs. 12a, b). Analyses on these STEM images reveal coherent strain states as well as interfacial coupling of OOR (Supplementary Figs. 12c, d), similar to the CRO/LCMO/CRO/NGO(110)$_O$ trilayer case. Importantly, the layer-resolved η_{LC} increases gradually from the bottom LCMO/NGO interface to the top surface (Supplementary Fig. 12d). The average value (black dashed line) (~170°) is closer to the bulk value and is higher than that in the CRO/LCMO/CRO/NGO(110)$_O$ trilayer (η_{LC}~167°). This result strongly suggests that the octahedral coupling at LCMO/CRO interfaces can effectively enhance the OOR of the LCMO layer in the trilayers, thus enhancing the monoclinic-like distortion as well as the IP-AHE.

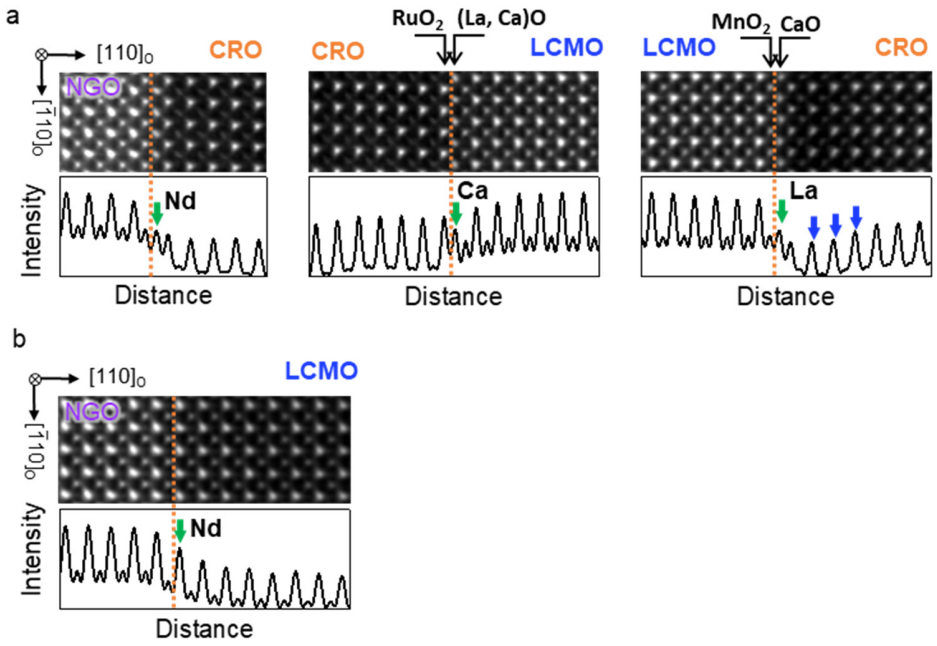

Supplementary Fig. 9 | STEM characterizations of the interfacial structures in the CRO/LCMO/CRO/ NGO(110)$_O$ trilayer heterostructure and LCMO/NGO(110)$_O$ thin film.

(a) HAADF-STEM images captured near the CRO/NGO(110)$_O$ interface, LCMO/CRO interface, and CRO/LCMO interface, viewed along the NGO [001]$_O$ axis. The bottom LCMO/CRO interface is terminated by RuO_2-(La,Ca)O configuration, while the top interface is terminated by the MnO_2-CaO configuration. **(b)** HAADF-STEM images captured near the LCMO/NGO(110)$_O$ interface of films without CRO. Both the LCMO/NGO(110)$_O$ interface and the CRO/NGO(110)$_O$ interface in the trilayer heterostructure are NdO-terminated.

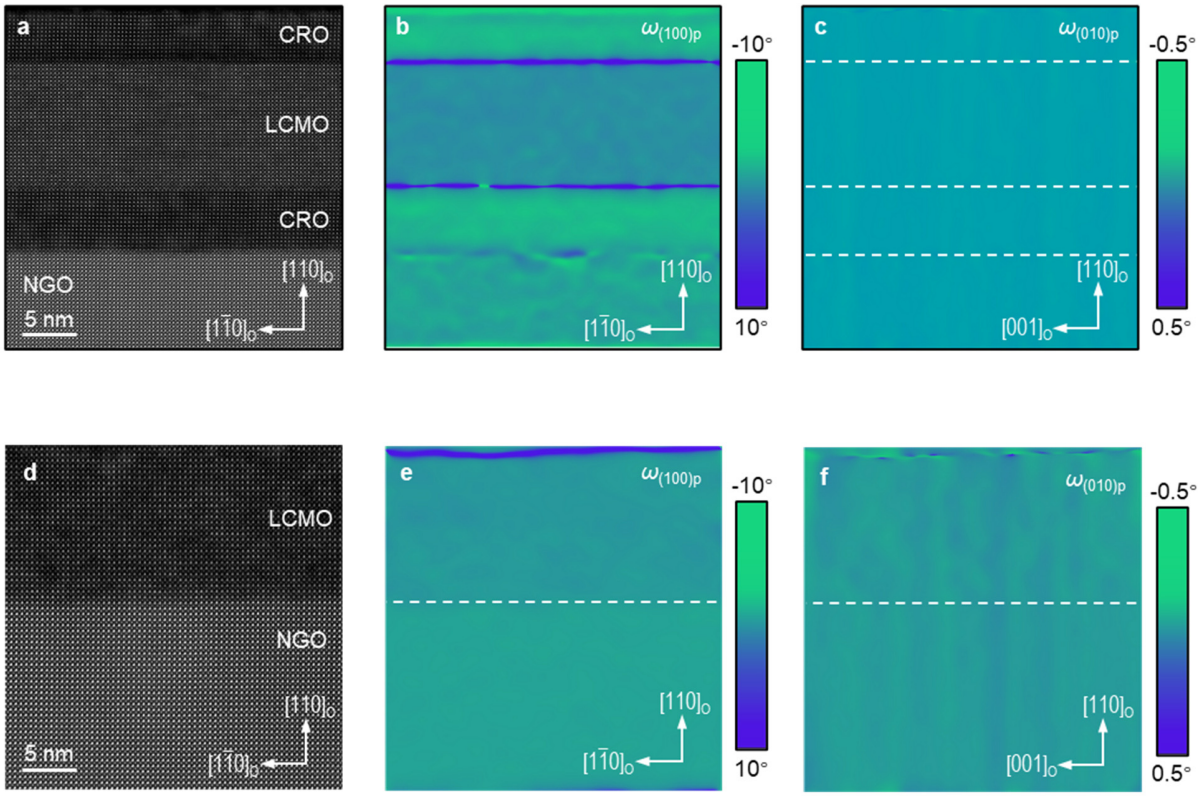

Supplementary Fig. 10 | GPA on the LCMO/NGO(110)$_O$ thin film and CRO/LCMO/CRO/NGO(110)$_O$ trilayer heterostructure.

(**a**) Large-scale HAADF-STEM image of the CRO(16 u.c.)/LCMO(32 u.c.)/CRO(16 u.c.)/NGO(110)$_O$ sample, viewed along the $[001]_O$ zone axis. (**b,c**) Geometric phase analysis (GPA) on the tilting of $(\bar{1}10)_O$ $[(100)_P]$ plane [defined as $\omega_{(100)P}$] (b) and $(001)_O$ $[(010)_P]$ plane [defined as $\omega_{(010)P}$] (c) of the CRO/LCMO/CRO/NGO(110)$_O$ trilayer. (**d**) Large-scale HAADF-STEM image of the LCMO(32 u.c.)/NGO(110)$_O$ thin film. (**e,f**) GPA on the $\omega_{(100)P}$ (e) and $\omega_{(010)P}$ (f) of the LCMO/NGO(110)$_O$ thin film. The color of the scale bar represents the different tilt directions and degrees of the pseudo-cubic unit-cells.

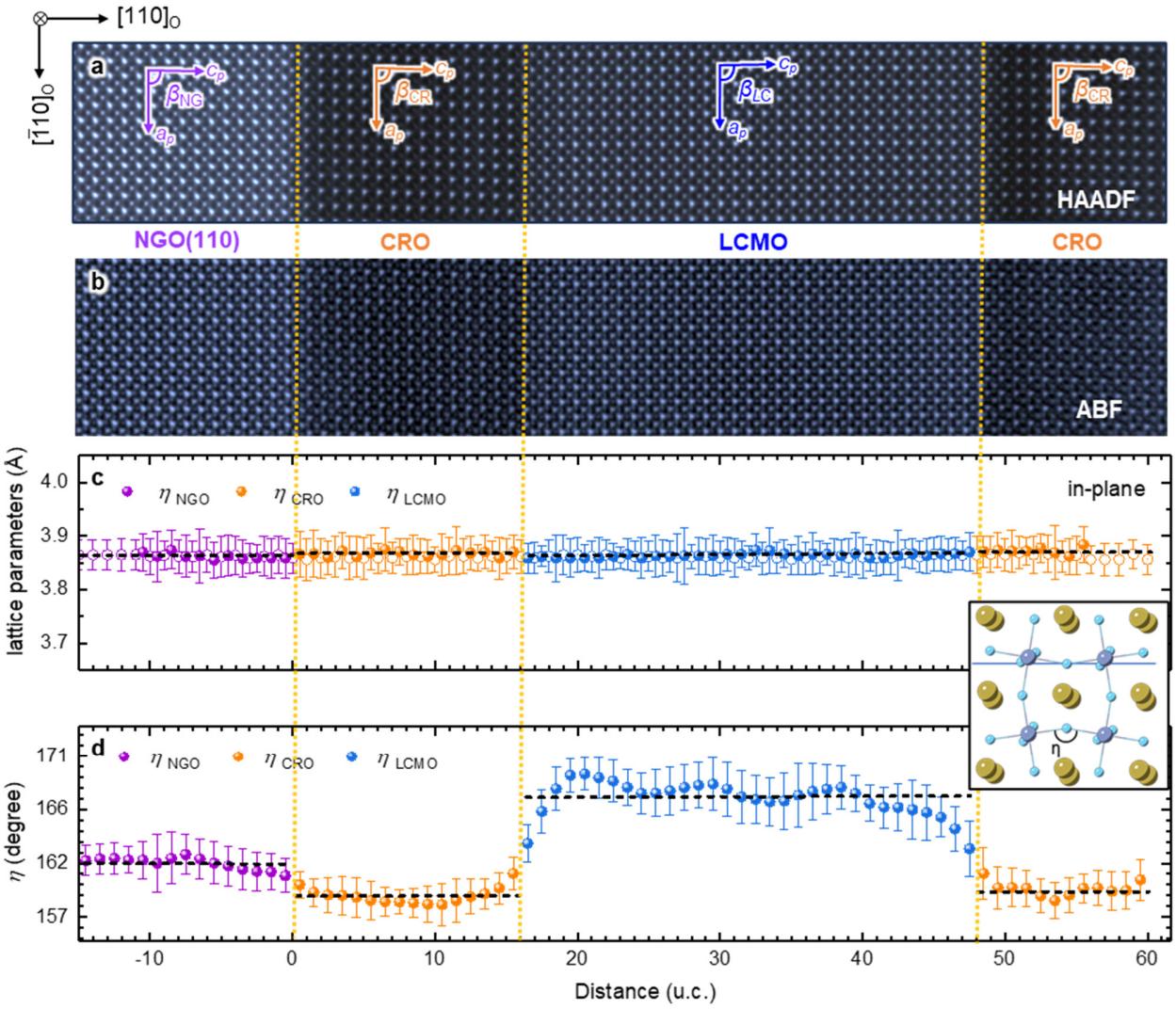

Supplementary Fig. 11 | Atomically-resolved STEM-HAADF and STEM-ABF images and corresponding analyses on the CRO/LCMO/CRO/NGO(110)$_O$ trilayers.

(**a**) An atomically-resolved STEM-HAADF image measured from a pre-selected area, marked by a white box in Fig. 2F. (**b**) STEM-ABF images corresponding to (a). (**c**) The in-plane lattice constants. (**d**) The bond angle η of each layer. η is shown in the inset diagram. The black dashed line segments are the average values.

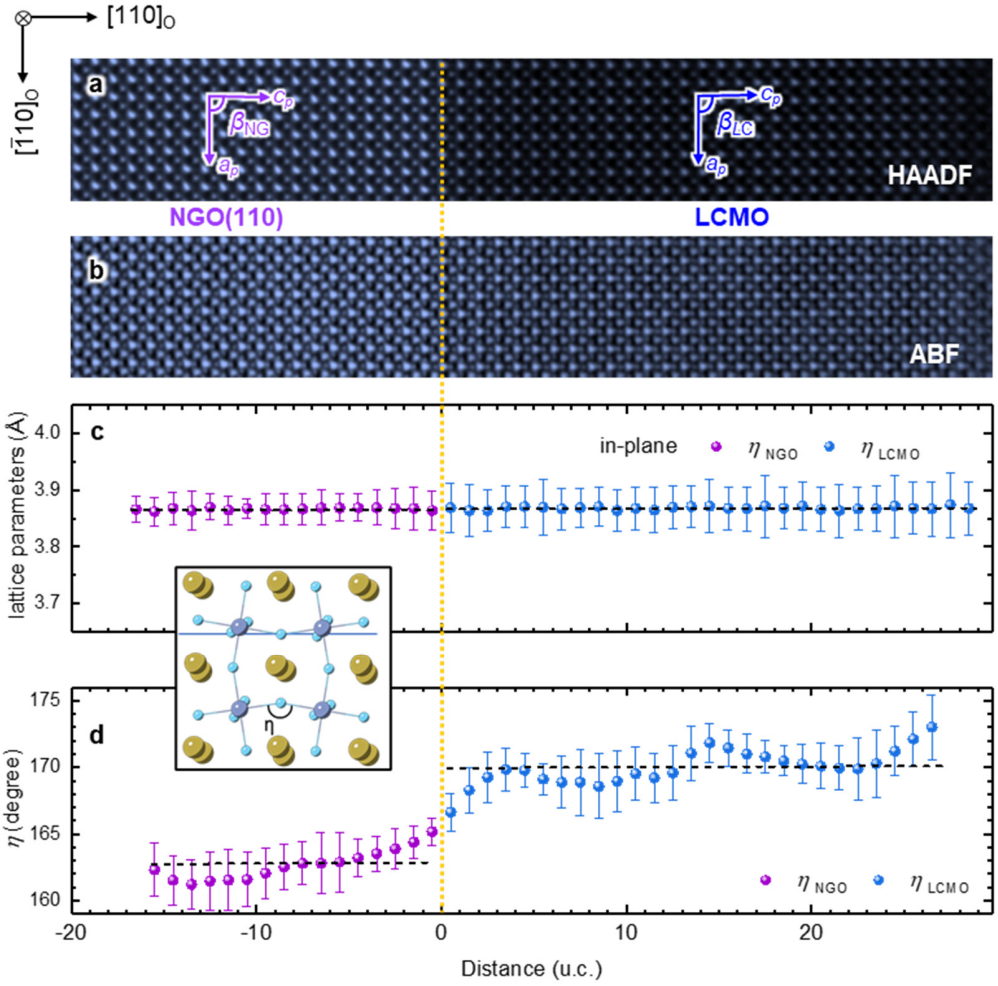

Supplementary Fig. 12 | Atomically-resolved STEM-HAADF and STEM-ABF images and corresponding analyses on the LCMO/NGO(110)$_O$ thin film.

(**a**) STEM-HAADF image and STEM-ABF image (**b**) of LCMO(32 u.c.) /NGO(110)$_O$ sample, viewed along the [001]$_O$ zone axis. (**c**) The in-plane lattice constants. (**d**) The bond angle η of each layer, η is shown in the inset diagram. The black dashed line segments are the average values.

Section 4. Additional IP-AHE measurements of CRO/LCMO/CRO/NGO(110)$_O$ trilayers

To verify that symmetry-controlled out-of-plane Berry curvature ($\bar{\boldsymbol{\Omega}}_z$) governs IP-AHE, we track the evolution of IP-AHE with the directions of transverse electric field ($\boldsymbol{E}$) and magnetic field vector ($\boldsymbol{H}$).

First, as depicted in Supplementary Fig. 13a, with fixed $\boldsymbol{E}//[\bar{1}10]_O$, we rotate the $\boldsymbol{H}$ vector in-plane (the angle between $\boldsymbol{H}$ and $\boldsymbol{E}$ is defined as θ), and measure the ρ_{AHE}-H curves (Supplementary Fig. 13b and Fig. 14). As summarized in Supplementary Fig. 13c,d, the θ-dependent ρ_{AHE} at $\boldsymbol{H}$ = 2000 Oe shows a typical cosine behavior: as the $\boldsymbol{H}$ vector rotates from the easy axis ($\boldsymbol{H}//[\bar{1}10]_O$, θ = 0° and 180°) to the hard axis ($\boldsymbol{H}//[001]_O$, θ = 90° and 270°), the saturated ρ_{AHE} ($\boldsymbol{H}$ = 2000 Oe) decreases gradually to zero, and the reversal of the $\boldsymbol{H}$ vector results in a sign-reversal of ρ_{AHE}. These results strongly suggest that only the in-plane $\boldsymbol{M}//[\bar{1}10]_O$ produces the IP-AHE. Taking the case of θ = 70° as an example (Supplementary Fig. 13e): when $\boldsymbol{H}$ is weak, the $\boldsymbol{M}$ initially aligns along the magnetic easy axis $[\bar{1}10]_O$, resulting in a relatively large ρ_{AHE}. As the $\boldsymbol{H}$ strength increases, the $\boldsymbol{M}$ vector gradually rotates toward the $\boldsymbol{H}$ direction, leading to a progressive reduction in ρ_{AHE}. The saturation ρ_{AHE} value should originate from the residual $\boldsymbol{M}$ component pinned to the easy axis $[\bar{1}10]_O$. Therefore, the ρ_{AHE}-θ curve displays a cosine-like line shape, which further reveals the mirror-symmetry-breaking-imposed dipolar structure of the $\bar{\boldsymbol{\Omega}}$ in spin-order space[17].

Second, as depicted in Supplementary Fig. 15a, with fixed $\boldsymbol{E}//[\bar{1}10]_O$, we also characterized the evolution of IP-AHE by rotating $\boldsymbol{H}$ within the cross-sectional $(001)_O$ plane (the angle between $\boldsymbol{H}$ and the film normal is defined as γ). We measured the ρ_{AHE}-H curves with variable γ and present the representative curves in Supplementary Fig. 15b (the full set of ρ_{AHE}-H curves is presented in Supplementary Fig. 16). In the case of $\boldsymbol{H}$ aligned along the film normal (γ = 0° and 180°), the curves display negligible ρ_{AHE}, which implies that the conventional AHE in the CRO/LCMO/CRO/NGO(110)o trilayer is negligible. For the other curves with variable γ, interestingly, the saturated ρ_{AHE} values for all the ρ_{AHE}-H curves are nearly identical, while the H_C value strongly depends on the γ angle. We further calculated the effective H projected in the plane by $H_{in} = H \sin\gamma$. The ρ_{AHE}-H_{in} curves for all the γ values exhibit almost identical H_C value and line shape (Supplementary Figs. 15c, d). These results further confirm that the conventional AHE contribution from out-of-plane H < 2500 Oe is negligible, and the observed IP-AHE under H < 1000 Oe should not originate from the out-of-plane component of misaligned in-plane $\boldsymbol{M}$.

Third, as depicted in Supplementary Fig. 17a, with fixed $\boldsymbol{H}//[\bar{1}10]_O$, we rotate the $\boldsymbol{E}$ in-plane (the angle between $\boldsymbol{E}$ and $[\bar{1}10]_O$ axis is defined as) by fabricating a series of Hall bars along different orientations (Supplementary Fig. 17b). The ρ_{AHE}-H hysteresis loops (Supplementary Fig. 17c) and the saturated ρ_{AHE} values (Supplementary Fig. 17d) are independent of φ, which is distinct from the planar Hall effect[18-20]. These results strongly suggest that the IP-AHE is dominated by the out-of-plane component of net Berry curvature ($\bar{\Omega}_z$): the nonzero $\bar{\Omega}_z$-induced $\boldsymbol{j}_{AHE}$ should be insensitive to the in-plane orientation of $\boldsymbol{E}$. This scenario is also well described by the Eq. 1 in the Main Text.

We also characterized the T-dependence of IP-AHE of CRO/LCMO/CRO trilayers. As shown in Supplementary Fig. 18, nonzero σ_{AHE} persists up to 200 K. Upon cooling, all of the σ_{AHE}-T curves exhibit a clear σ_{AHE} increment at T < 80 K, consistent with the reduction of ρ_{xx}. For the trilayer samples with relatively weak IP-AHE ($t_{CRO} \geq$ 32 u.c. or $t_{CRO} \leq$ 8 u.c.), σ_{AHE} reverses sign from negative to positive near 100 K upon warming. Such a sign-reversal behavior is similar to the intrinsic AHE of SRO thin films, which is sensitive to the band topology.

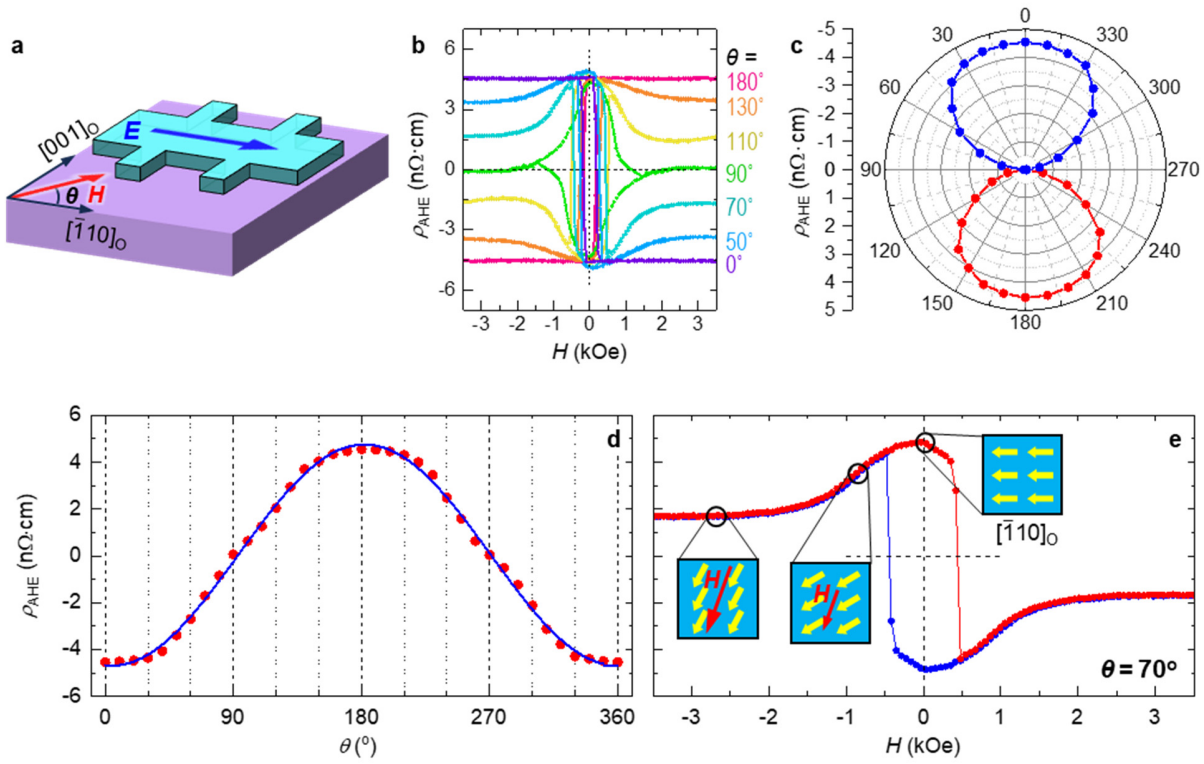

Supplementary Fig. 13 | IP-AHE measurements with in-plane *H*-rotation geometry.
(**a**) Schematic illustrations of IP-AHE measurements with in-plane *H*-rotation geometry: we fix the applied ***E*** direction along LCMO[$\bar{1}$10]$_O$ axis (a_p-axis), and rotate ***H*** vector in the LCMO(110)$_O$ plane. The angle between ***H*** and LCMO[$\bar{1}$10]$_O$ axis is defined as θ. (**b**) ρ_{AHE}-H curves measured from the CRO(16 u.c.)/LCMO(32 u.c.)/CRO(16 u.c.)/NGO(110)$_O$ sample in in-plane H-rotation geometry with variable θ values. (**c,d**) Polar-plot (c) and linear plot (d) of saturated ρ_{AHE} (ρ_{AHE} at H = 2000 Oe) versus θ. (**e**) A representative ρ_{AHE}-H curve measured with in-plane H-rotation geometry at θ = 70°. The inset illustration depicts the magnetization states under different H strengths.

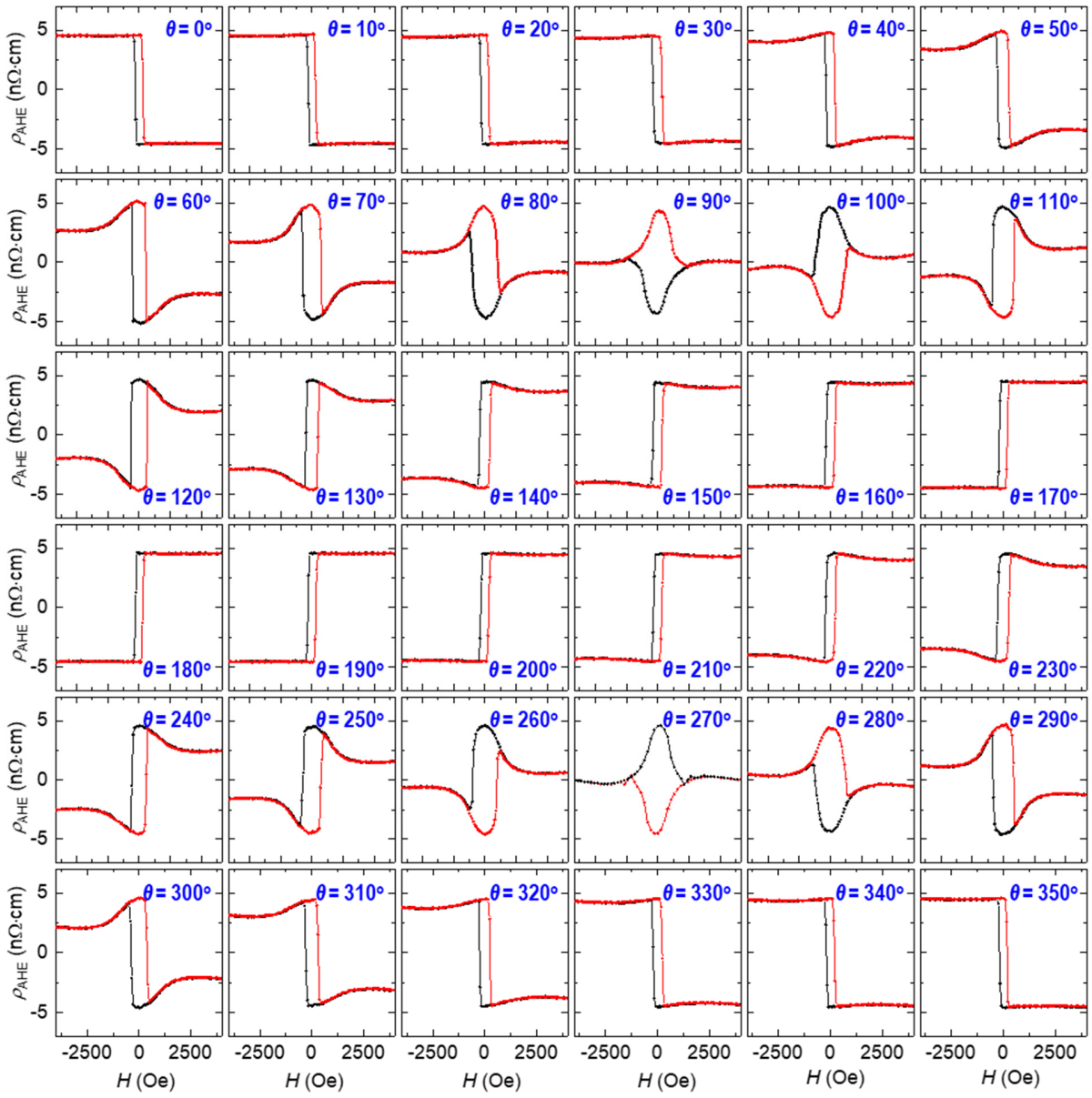

Supplementary Fig. 14 | Full set of ρ_{AHE}-H curves measured with in-plane H-rotation geometry. ρ_{AHE}-H curves measured from the CRO(16 u.c.)/LCMO(32 u.c.)/CRO(16 u.c.)/NGO(110)$_O$ sample in in-plane H-rotation geometry with variable θ values, ranging from 0° to 350° in 10° steps.

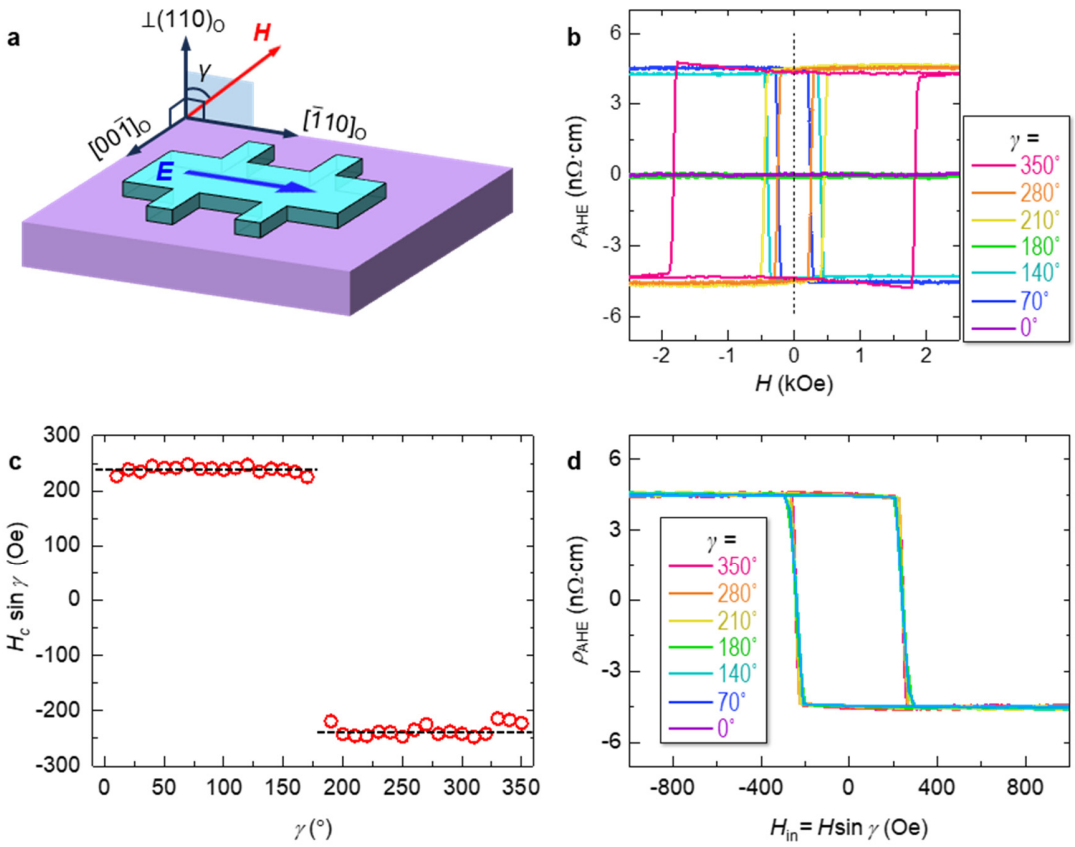

Supplementary Fig. 15 | IP-AHE measurements with out-of-plane *H*-rotation geometry.
(**a**) Schematic illustrations of IP-AHE measurements with out-of-plane *H*-rotation geometry: we fix the applied ***E*** direction along LCMO$[\bar{1}10]_O$ axis (a_p-axis), and rotate ***H*** vector in the LCMO$(001)_O$ plane. The angle between ***H*** and the film normal is defined as γ. (**b**) The ρ_{AHE}-H curves measured from the CRO(16 u.c.)/LCMO(32 u.c.)/CRO(16 u.c.)/NGO$(110)_O$ sample in out-of-plane H-rotation geometry with variable γ. (**c**) The effective H projected in plane by $H_{in} = H \sin\gamma$. (**d**) The ρ_{AHE}-H_{in} curves with variable γ values.

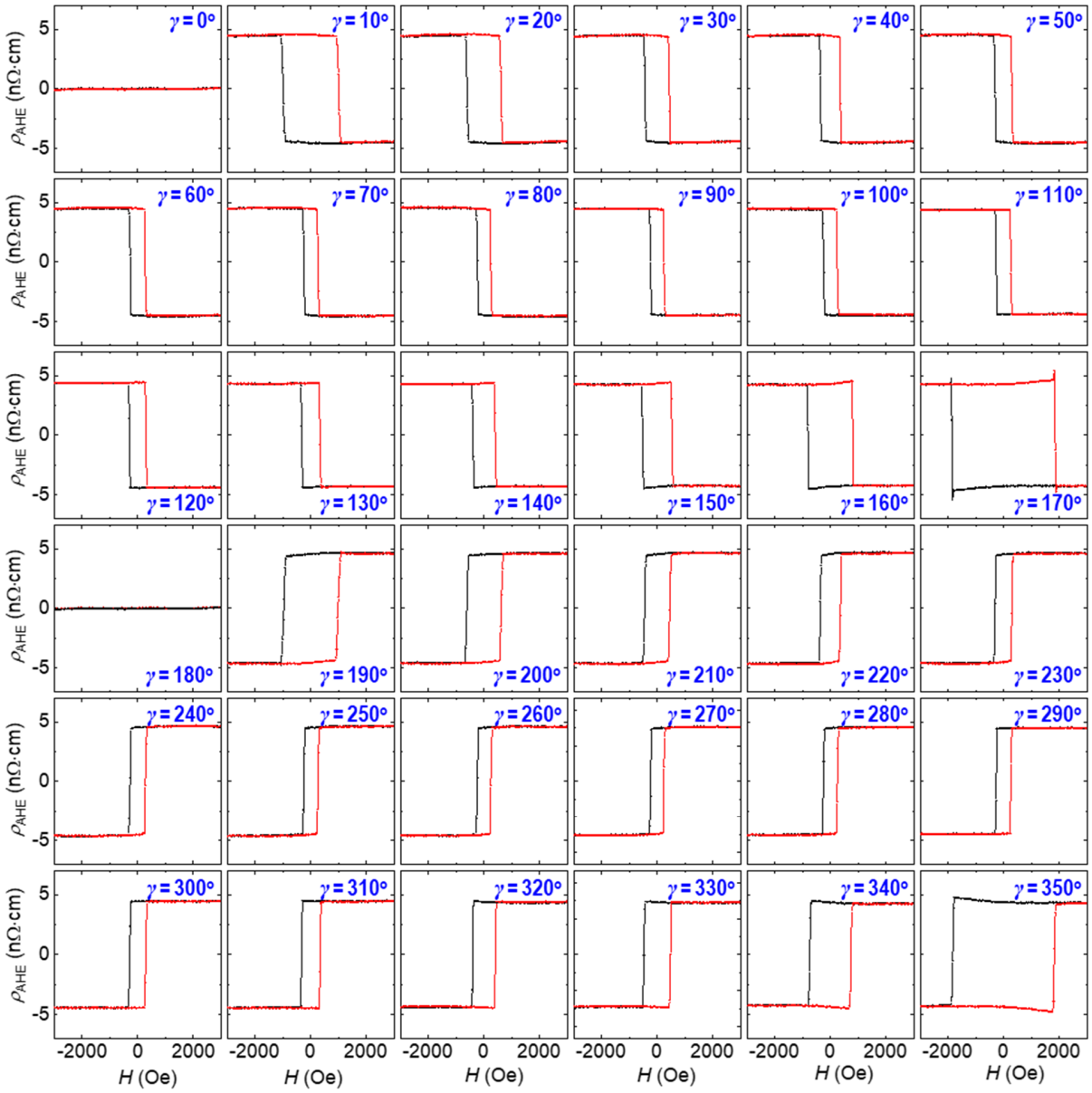

Supplementary Fig. 16 | Full set of ρ_{AHE}-H curves measured with out-of-plane H-rotation geometry. ρ_{AHE}-H curves measured from the CRO(16 u.c.)/LCMO(32 u.c.)/CRO(16 u.c.)/NGO(110)$_O$ sample in out-of-plane H-rotation geometry with variable γ values, ranging from 0° to 350° in 10° steps.

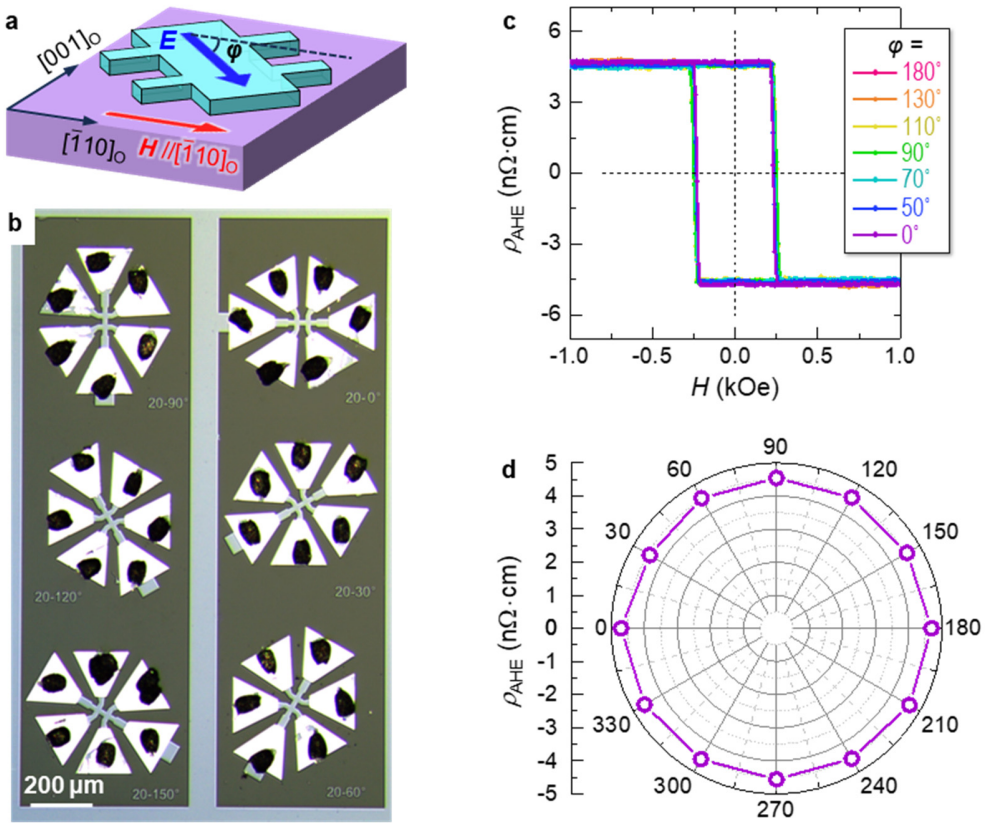

Supplementary Fig. 17 | IP-AHE measurements with in-plane *E*-rotation geometry.
(**a**) Schematic illustrations of IP-AHE measurements with *E*-rotation geometry: We fix the ***H*** vector along LCMO[$\bar{1}$10]$_O$ axis, and rotate the ***E*** in the LCMO(110)$_O$ plane. The angle between ***E*** and LCMO[$\bar{1}$10]$_O$ axis is defined as φ. (**b**) Optical images of Hall bars with different rotation directions, and the angle between the Hall bar current direction and ($\bar{1}$10)$_O$ is φ (φ = 0°, 30°, 60°, 90°, 120°, 150°). The white line represents a scale bar of 200 μm. (**c**) ρ_{AHE}-H curves measured from the CRO(16 u.c.)/LCMO(32 u.c.)/CRO(16 u.c.)/NGO(110)$_O$ sample in E-rotation geometry with variable φ values. (**d**) Polar-plot of saturated ρ_{AHE} versus φ.

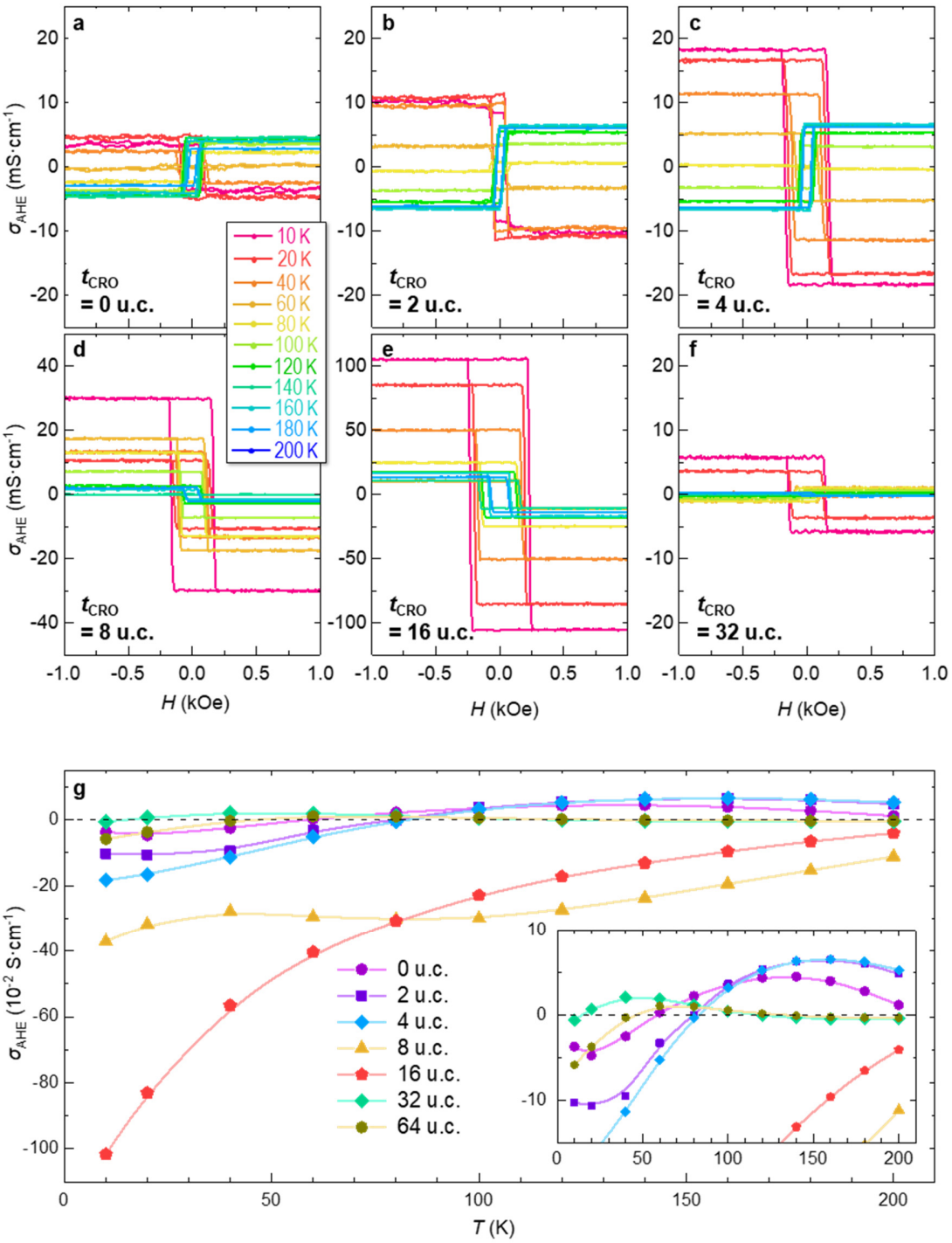

Supplementary Fig. 18 | σ_{AHE} -H curves measured at variable temperatures.
(**a-f**) σ_{AHE}-H curves of CRO(t_{CRO})/LCMO(32 u.c.)/CRO(t_{CRO})/NGO(110)$_O$ trilayers measured at various T for t_{CRO} = 0 u.c. (a), 2 u.c. (b), 4 u.c. (c), 8 u.c. (d), 16 u.c. (e), 32 u.c. (f). (**g**) Temperature-dependent σ_{AHE} (σ_{AHE}-T) curves of CRO/LCMO/CRO/NGO(110)$_O$ heterostructures with various t_{CRO}. The inset is a zoom-in plot of σ_{AHE}-T curves for highlighting the sign changes of σ_{AHE}.

Section 5. Additional DFT calculation results.

To uncover the electronic origin of the IP-AHE, we employ density-functional theory (DFT) combined with Wannier function projection to calculate the electronic structure near the Fermi level, the Berry curvature, and the AHE conductivity. The computational methods and details are provided in the *Methods* section ("Density-functional theory calculations"). We note that all calculations in this study are performed on LCMO structures with and without octahedral rotations/tilts and lattice distortions, while the CRO buffer layer, which imposes different OOR in LCMO experimentally, is omitted. Including the substrate in band-structure and Wannier projections—together with SOC, Hubbard-U corrections, and ferromagnetic spin splitting—would dramatically increase the computational cost and hinder convergence. Therefore, balancing computational feasibility and reliability, as shown in Supplementary Figs. 19a-d, we construct the four different $(110)_O$-oriented LCMO 2×2×2 supercells: one high-symmetry cubic supercell without any OOR and three orthorhombic supercells with $a^-a^-c^+$-type OOR and Jahn-Teller distortion. The variable amplitudes of OOR and Jahn-Teller distortions in the orthorhombic supercells give rise to variable β_{LC} = 90.0°, 90.08°, and 90.16°. Supplementary Figs. 20a-d present the DFT band structures and the Wannier-interpolated band structures for all four supercells. The Wannier Hamiltonians include SOC, Hubbard-U, and ferromagnetic exchange splitting. The close agreement between the Wannier-interpolated bands and the DFT results, particularly within the energy window from −1 to 2 eV around the Fermi level. This agreement validates the subsequent Berry curvature and AHE conductivity calculations.

Using the optimized LCMO supercells with variable OOR patterns, we further calculate the net Berry curvature $\bar{\boldsymbol{\Omega}}$ and the corresponding anomalous Hall conductivities σ_{xy}, σ_{yz}, and σ_{xz} (Supplementary Fig. 21). The x, y, and z axes are defined as $x//[\bar{1}10]_O$, $y//[001]_O$, and $z\perp(110)_O$. For all the calculations, the $\boldsymbol{M}$ vector is imposed along the x-axis (LCMO$[\bar{1}10]_O$ axis). The σ_{xy}, induced by the out-of-plane component of $\bar{\boldsymbol{\Omega}}$ ($\bar{\Omega}_z$) is consistent with our experimental measurement geometry. Therefore, we extract the k-dependent $\bar{\Omega}_z$ in Supplementary Figs. 20e-h. We denote the DFT-calculated σ_{xy} as σ_{DFT} in the Main Text. For the cubic LCMO supercell (Supplementary Fig. 21a), $\bar{\Omega}_z$ is close to zero, leading to $\sigma_{xy} = 0$ at the Fermi surface (E_F). Namely, the IP-AHE is prohibited by the cubic symmetry. In contrast, for these orthorhombic LCMO supercells, additional k-points in the Brillouin zone result in finite $\bar{\Omega}_z$ and a nonzero σ_{xy} at the E_F. The magnitude of σ_{xy} increases monotonically with β_{LC}, consistent with the experimental trend. These results demonstrate the essential roles of octahedral rotation/tilt and monoclinic-like distortion (i.e., $\beta_{LC} \neq 90°$) for activating the in-plane AHE.

Guided by the experimental results shown in Fig. 3, we further evaluate the evolution of the DFT calculated IP-AHE with the orientation of the in-plane $\boldsymbol{M}$ vector. As shown in Supplementary Fig. 22a, we conduct the DFT calculation on σ_{xy} by rotating the $\boldsymbol{M}$ vector within the $(110)_O$ plane (the angle between $\boldsymbol{M}$ and LCMO$[\bar{1}10]_O$ axis is defined as θ). As the $\boldsymbol{M}$ vector rotates from the $[\bar{1}10]_O$ axis to the $[001]_O$ axis, the σ_{xy} values decrease gradually to zero, which further confirms the critical role of uniaxially-polarized ferromagnetism in activating IP-AHE.

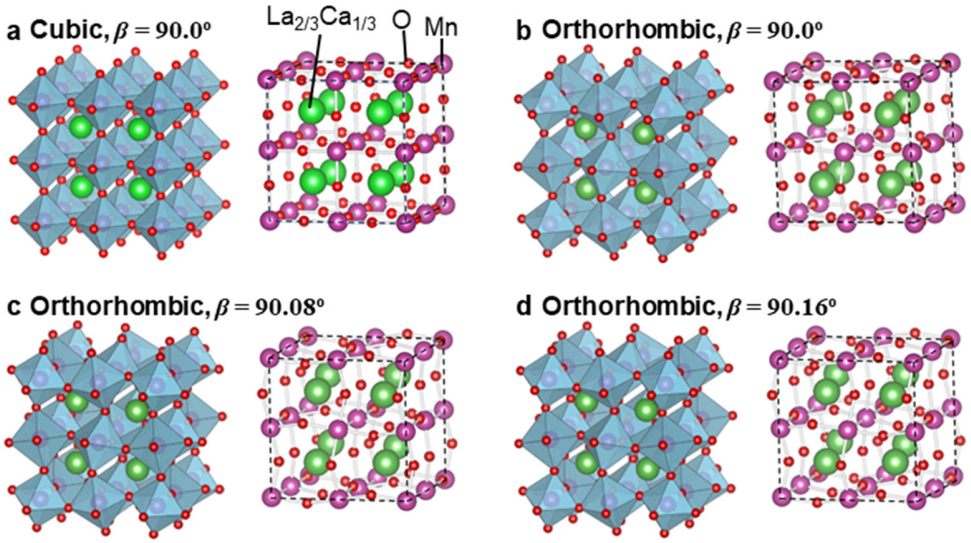

Supplementary Fig. 19 | LCMO supercells for DFT calculation.
(**a**) Schematic illustrations of the cubic LCMO 2×2×2 supercells without any octahedral rotation. (**b-d**) Schematic illustrations of orthorhombic LCMO 2×2×2 supercells with variable $a^-a^-c^+$ octahedral rotation pattern, leading to unequal monoclinic tilting angles β_{LC} = 90.00° (b), 90.08° (c), and 90.16° (d). The left panels highlight the MnO_6 octahedral network, with Mn atoms (green spheres) coordinated by oxygen atoms (red spheres). The right panels highlight the atomic positions within the unit-cells.

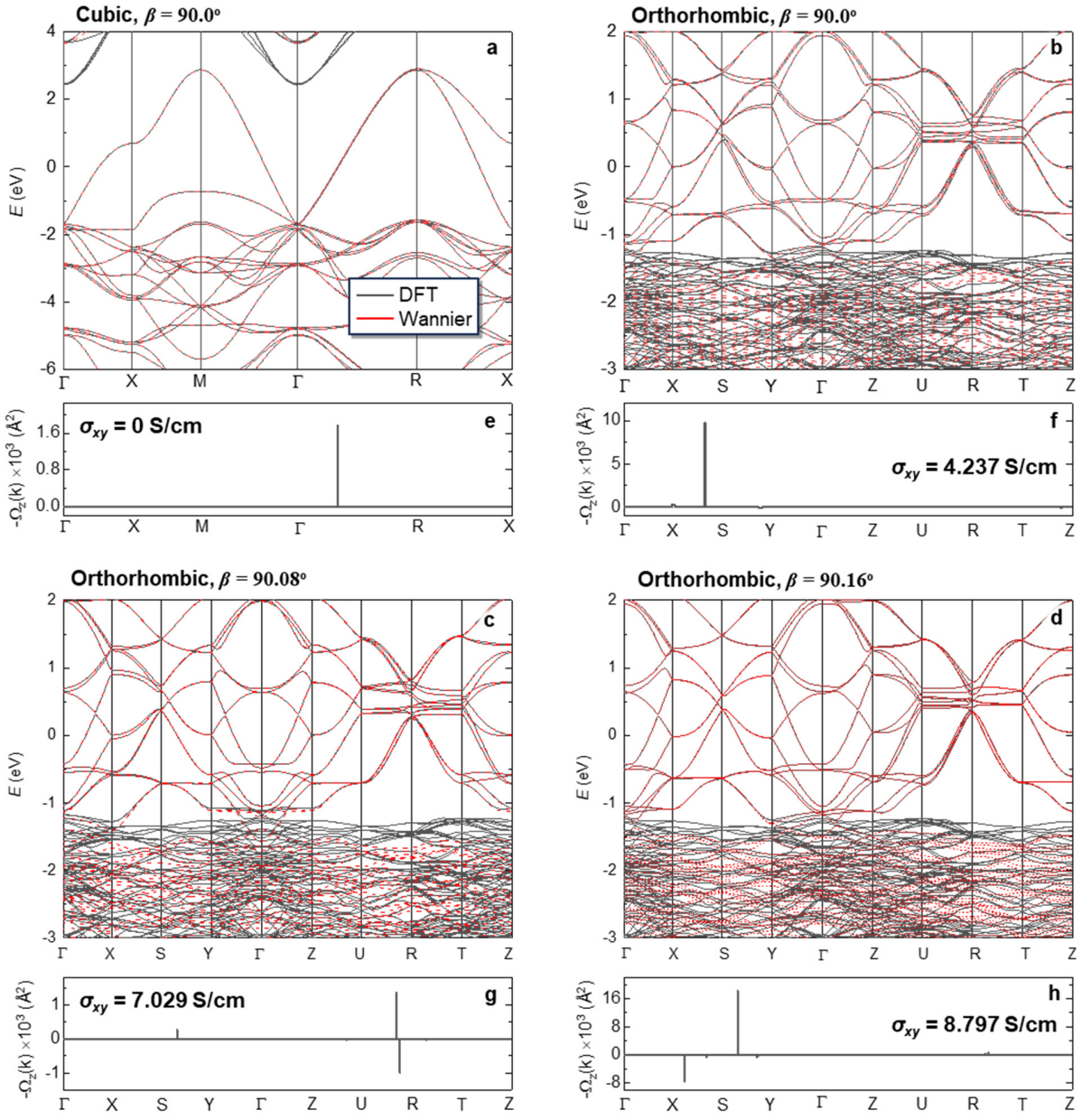

Supplementary Fig. 20 | DFT-calculated band structures and corresponding out-of-plane Berry curvature of cubic and orthorhombic LCMO supercells.

(**a**-**d**) DFT-calculated band structure (black lines) and corresponding Wannier projections (tight-binding bands: red lines) of (a) cubic supercell with β_{LC} = 90.0°, (b) orthorhombic supercell with β_{LC} = 90.0°, (c) orthorhombic supercell with β_{LC} = 90.08°**,** and (d) orthorhombic supercell with β_{LC} = 90.16°. (**e**-**h**) The corresponding *k*-dependent Berry curvature $\Omega_z(k)$ along the same *k*-path (as in the DFT and Wannier bands). The DFT-calculated anomalous Hall conductivity σ_{xy} values are also labeled in (e-h).

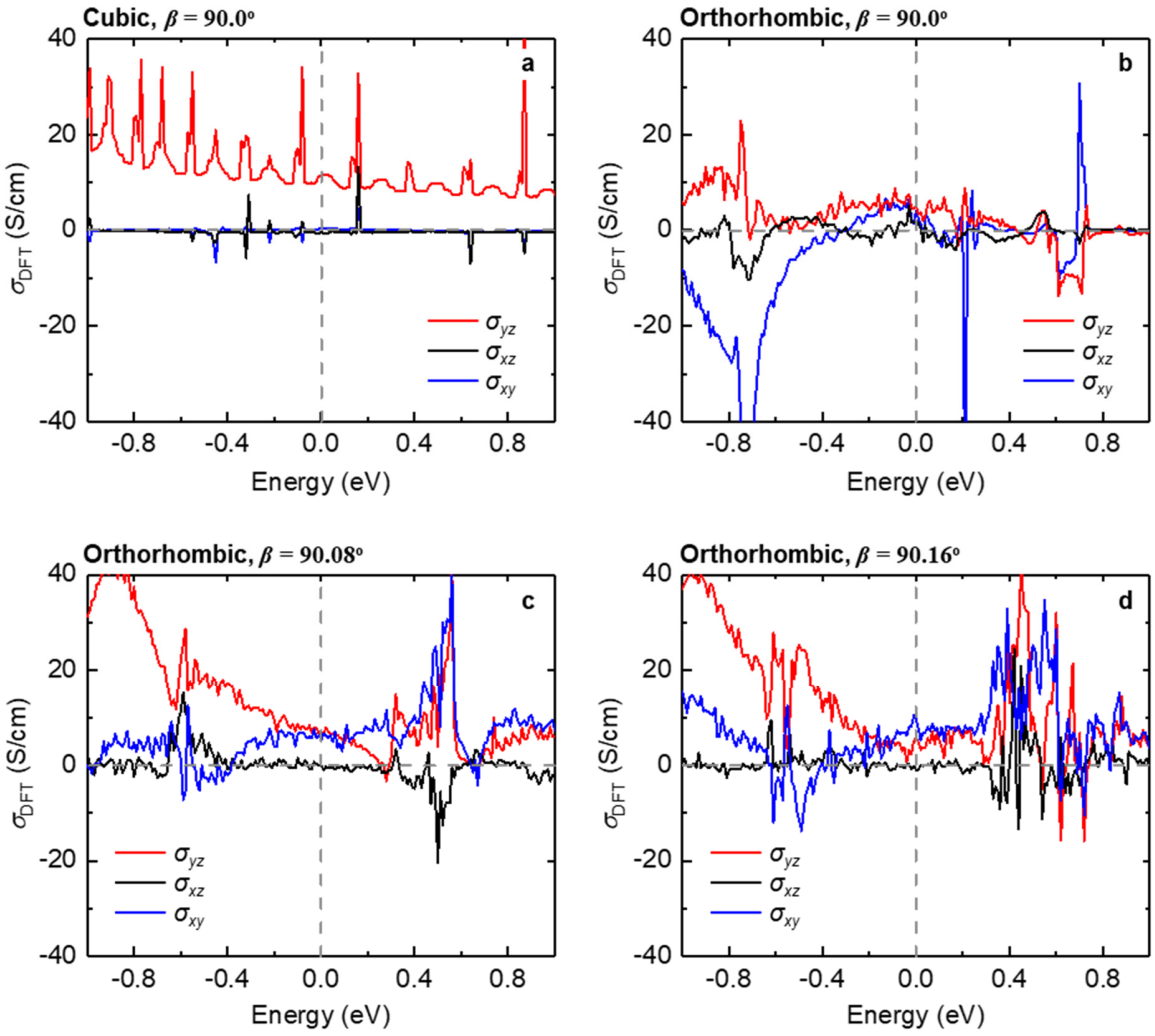

Supplementary Fig. 21 | DFT-calculated anomalous Hall conductivity of LCMO supercells.

(**a-d**) Anomalous Hall conductivity (σ_{DFT}) calculated by DFT(+U+SOC) and Wannier projections of (a) ideal cubic LCMO supercell and (b-d) orthorhombic LCMO supercell with variable OOR pattern and β_{LC} angles. For the cubic LCMO supercell, σ_{xy} (blue line) and σ_{xz} (black line) are strictly equal to zero at the Fermi level (E_F), reflecting preserved D_4 symmetry. For the orthorhombic LCMO supercells (σ_{xy}, blue line; σ_{xz}, black line, and σ_{yz}, red line), as β deviates from 90°, all the off-diagonal conductivity components become nonzero, indicating symmetry breaking and emergence of IP-AHE.

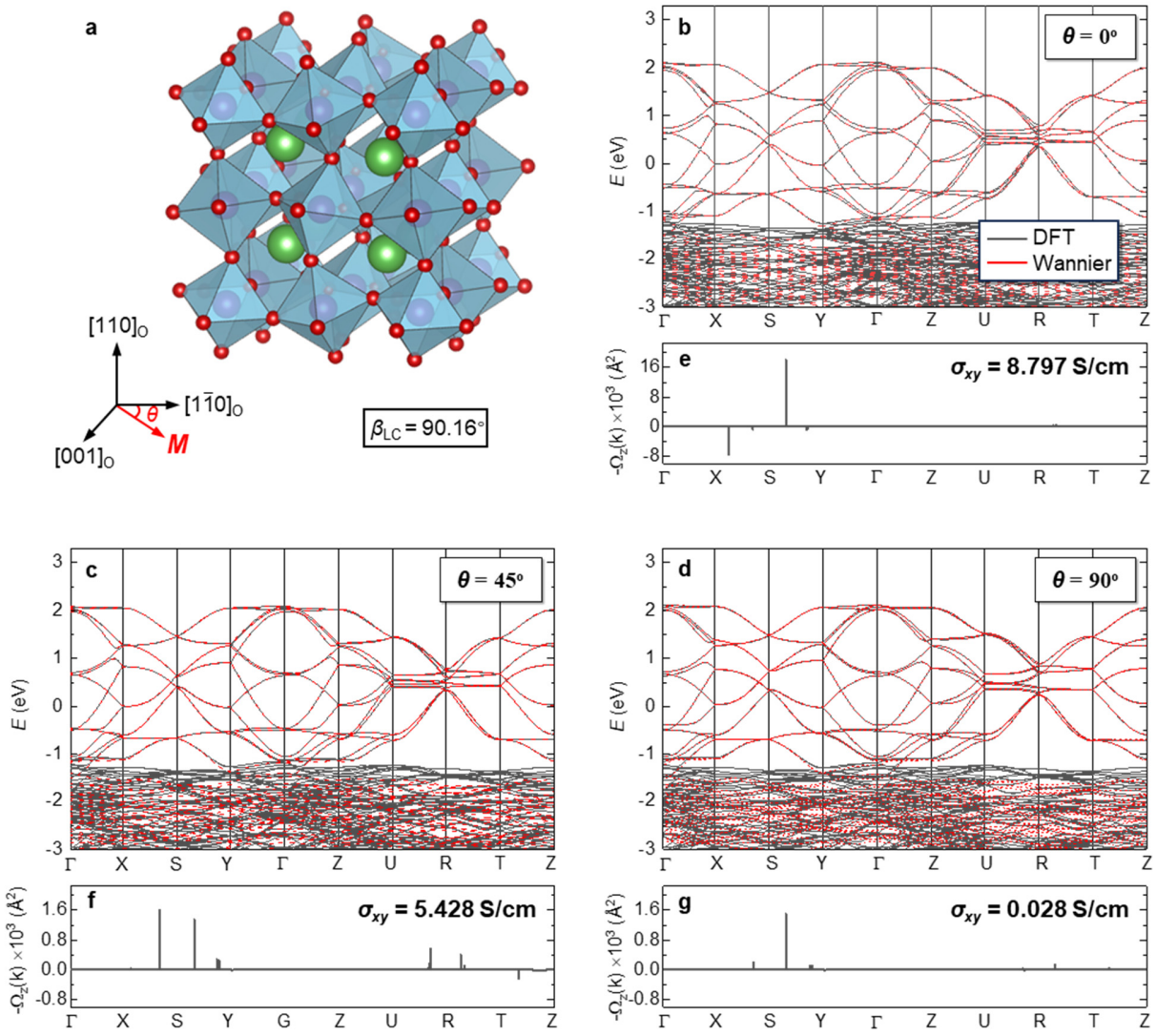

Supplementary Fig. 22 | DFT-calculated band structures and corresponding out-of-plane Berry curvature with variable *M* vectors.

(**a**) Schematic illustrations of orthorhombic LCMO 2×2×2 supercells with $a^-a^-c^+$ OOR pattern and monoclinic tilting angle β_{LC} = 90.16°. (**b-d**) DFT-calculated band structure (black lines) and corresponding Wannier projections (tight-binding bands: red lines) of orthorhombic supercell illustrated in (a), with ***M*** vector rotated in the LCMO(110)$_O$ plane (the angle between the in-plane ***M*** and the $[\bar{1}10]_O$ axis is defined as θ). (e-g) The corresponding k-dependent $\Omega_z(k)$ along the same k-path (as in the DFT and Wannier bands). The DFT-calculated anomalous Hall conductivity σ_{xy} values are also labeled in (e-g).

Section 6. Supporting results and DFT calculations related to ionic liquid gating of IP-AHE

As demonstrated in Fig. 4 in the Main Text, ionic liquid gating (ILG) serves as an effective tuning knob for the IP-AHE. In this section, we show supporting results related to the reversible nature of ILG and DFT calculations on the proton intercalation process at the atomic scale.

We first verify the reversible nature of this ILG control of IP-AHE. In the ILG experiment, we gradually increase the gate voltage (V_g) from 0 to +1.5 V, and the in-plane anomalous Hall conductivity (σ_{AHE}) gradually decreases from 103.7 mS/cm to zero at $V_g \geq +1.4$ V (Fig. 4c). We then reduce V_g back to 0 and observe a recovery of zero-field σ_{AHE} to ~ 96.3 mS/cm (f Supplementary Fig. 23, step 1st), strongly suggesting that the protonation-induced suppression of IP-AHE is volatile at room temperature. Upon further applying a negative V_g of −1.0 V, the zero-field σ_{AHE} reaches 103.3 mS/cm (Supplementary Fig. 23, step 2nd), which is close to the pristine value before ILG. Subsequently, by alternatively applying positive V_g = +1.4 V and negative V_g = −1.0 V, we observe highly reversible activation and suppression of IP-AHE (Supplementary Fig. 23, step 3rd-10th).

Based on these results and previous literature[16, 21], we speculate that proton intercalation under positive V_g induces structural transformations in the CRO/LCMO/CRO/NGO(110)$_O$ trilayer heterostructure. We further expect that the associated changes in structural symmetry dominate the modulation of IP-AHE. To clarify the structural evolution during protonation, we measure XRD 2θ-ω scans from a 24 nm-thick CRO/NGO(110)$_O$ thin film (Supplementary Fig. 24a) and a 32 nm-thick LCMO/NGO(110)$_O$ thin film (Supplementary Fig. 24b). For both films, the pristine 2θ-ω curve measured before ILG displays well-defined Laue fringes, confirming the high epitaxial quality. Notably, neither curve shows separated LCMO and CRO peaks, due to the nearly identical peak positions of LCMO(440)$_O$, CRO(440)$_O$, and NGO(440)$_O$ diffractions. After covering the sample surface with ionic liquid, the diffraction intensities of both CRO(440)$_O$ and LCMO(440)$_O$ decrease slightly due to enhanced X-ray scattering. To reliably resolve the structural evolution during ILG, we wait for 5 minutes at each V_g and then perform XRD 2θ–ω measurements without turning off the V_g.

The ILG-induced protonation process can trigger considerable changes in XRD 2θ-ω linear scans of both CRO and LCMO films. For the CRO/NGO(110)$_O$ thin film, 2θ-ω linear scans barely change as V_g increases from 0 to +1.0 V. When V_g exceeds the threshold value of +1.1 V, the CRO(440)$_O$ peak shifts towards a lower Bragg angle, signifying an out-of-plane lattice expansion of CRO during protonation. This peak shift tends to saturate as V_g approaches +1.5 V. After completing the gating sequence up to V_g = +1.6 V, we reduce V_g to 0 and then apply a negative V_g = −1.0 V. The CRO(440)$_O$ peak surprisingly shifts back to its pristine position, confirming that the protonation-induced structural transformation in CRO is highly reversible. In sharp contrast, the LCMO/NGO(110)$_O$ thin film undergoes structural transformation only above a much higher threshold V_g = +2.2 V. As V_g increases further to +3.4 V, the LCMO(440)$_O$ peak continuously shifts toward higher Bragg angles and becomes substantially broader, suggesting a high degree of structural inhomogeneity during protonation. After reducing the V_g to 0, the significantly broadened and shifted LCMO(440)$_O$ diffraction peak remains nearly unchanged. Accordingly, the protonation process in the LCMO layer should be essentially irreversible.

Taken together, the XRD results indicate that CRO and LCMO films exhibit distinct structural evolutions under ILG. In CRO, the protonation-induced structural transformation exhibits a low threshold V_g ~ +1.1

V, quickly saturates at V_g = +1.5 V, and is reversible when turning off V_g. This behavior closely resembles the V_g-dependent ILG control of IP-AHE (Fig. 4c in the Main Text and Supplementary Fig. 23). In contrast, the protonation-induced structural transformation in the LCMO layer occurs only in much higher $V_g \sim +2.2$ V, is irreversible, and does not readily saturate. Accordingly, during ILG of our CRO/LCMO/CRO trilayer, the sharp changes in σ_{AHE} at +1.1 V ≤ V_g ≤ +1.4 V should be primarily accompanied by the proton intercalation occurring first in the CRO layers, forming an H_xCaRuO_3 phase[22]. Due to the high threshold V_g, the LCMO layer in the CRO/LCMO/CRO trilayer should not undergo any detectable macroscopic structural changes during the ILG, which is consistent with the nearly unchanged coercive field (H_C) observed in Fig. 4c and Supplementary Fig. 23.

To reveal the symmetry modulations of the CRO/LCMO/CRO trilayer during ILG, we conducted DFT calculations on the protonation-induced structural changes in CRO. In the DFT-level structural optimization, we construct H_xCaRuO_3 supercells (x = 0, 0.25, 0.5, 1.0) following the details described in Ref. 22 and then perform structural relaxations. The gradually increased H concentration in H_xCaRuO_3 can reproduce the protonation process during ILG under V_g < +1.5 V. The atomic structures of pristine CRO and proton-intercalated H_xCaRuO_3 supercells, viewed along the $[\bar{1}10]_O$ axis, are depicted in Supplementary Fig. 25. The vertical distance between two Ru cations ($d_{Ru\text{-}Ru}$, corresponding to the c_p value) and the out-of-plane Ru-O-Ru bond angle $\eta_{Ru\text{-}O\text{-}Ru}$, extracted from these supercells, are summarized in Supplementary Fig. 26. The DFT calculations have revealed three critical structural modulations during protonation: 1) The intercalated proton ions prefer to bond the equatorial oxygen ions in RuO_6 octahedra; 2) The $d_{Ru\text{-}Ru}$ increases gradually with H concentration x, which is consistent with the peak shift of $CRO(220)_O$ diffraction; 3) The Ru-O-Ru bond angle $\eta_{Ru\text{-}O\text{-}Ru}$ increases gradually with H concentration x, which signify a suppression of out-of-plane anti-phase tilting of RuO_6 octahedra and the orthorhombicity d_{OR}. According to the strong coupling of octahedral rotation/deformation at the LCMO/CRO interface, we expect that the protonation-induced suppression of CRO can further suppress the tilting and deformation of MnO_6 octahedra in the LCMO layer. To test this scenario, we further conduct DFT calculations on the H_xCaRuO_3/LCMO bilayer supercell with gradually increasing H concentration x (Supplementary Fig. 27). Although the H atoms still bond to the equatorial oxygen ions of the RuO_6 octahedra in CRO, the Mn-O-Mn bond angle ($\eta_{Mn\text{-}O\text{-}Mn}$) and the corresponding octahedral tilting are also gradually suppressed as H concentration increases, consistent with the scenario of interfacial octahedral coupling. Therefore, the associated control of monoclinic-like distortion and symmetry lowering in LCMO could be the main driving force of the observed modulation of IP-AHE during ILG.

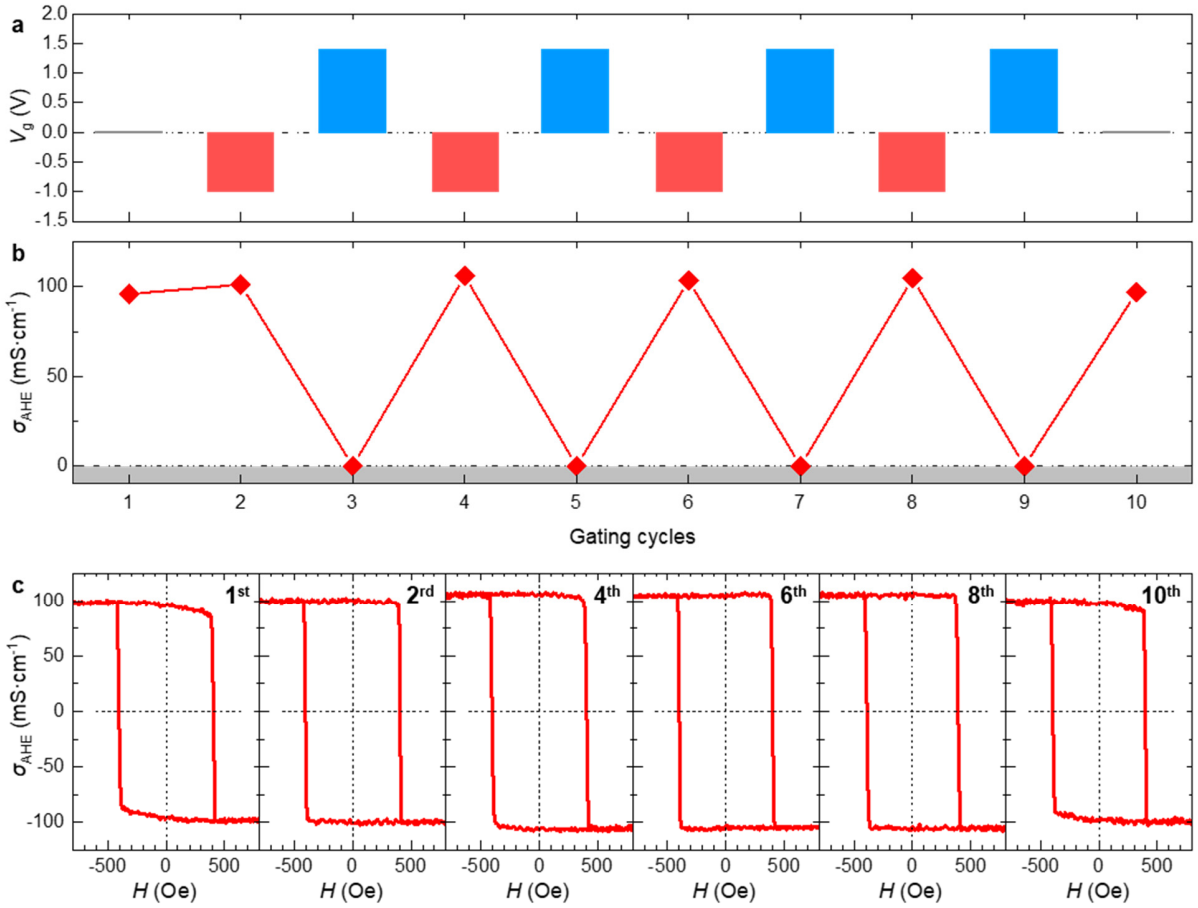

Supplementary Fig. 23 | Reversible ILG of IP-AHE in CRO/LCMO/CRO/NGO(110)$_O$ trilayer.
(**a**) V_g applied during 10 ILG steps. (**b**) Summary of σ_{AHE} at zero field during the 10 ILG steps with variable V_g. The curve clearly displays a reversible suppression/activation of IP-AHE by applying positive/negative V_g. (**c**) σ_{AHE}-H curves measured after the ILG step 1, 2, 4, 6, 8, and 10. These consistent and similar hysteresis loops further corroborate that the ILG of IP-AHE is reversible.

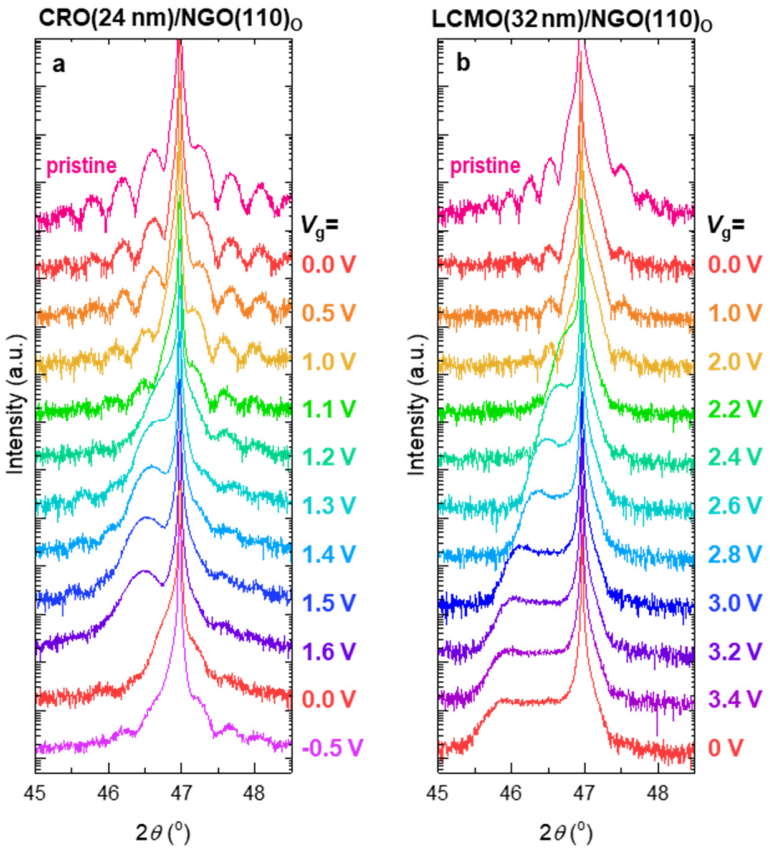

Supplementary Fig. 24 | XRD characterizations of CRO and LCMO thin films during ILG.
(**a**) XRD 2θ-ω linear scans measured from 24 nm-thick CRO/NGO(110)$_O$ thin film during ILG under gradually increasing V_g from 0 to +1.6 V. The 2θ-ω linear scans acquired after reducing the V_g to 0 and -0.5 V are also acquired. (**b**) XRD 2θ-ω linear scans measured from 32 nm-thick LCMO/NGO(110)$_O$ thin film during ILG under gradually increasing V_g from 0 to +3.4 V. The 2θ-ω linear scans are also acquired after reducing the V_g to zero.

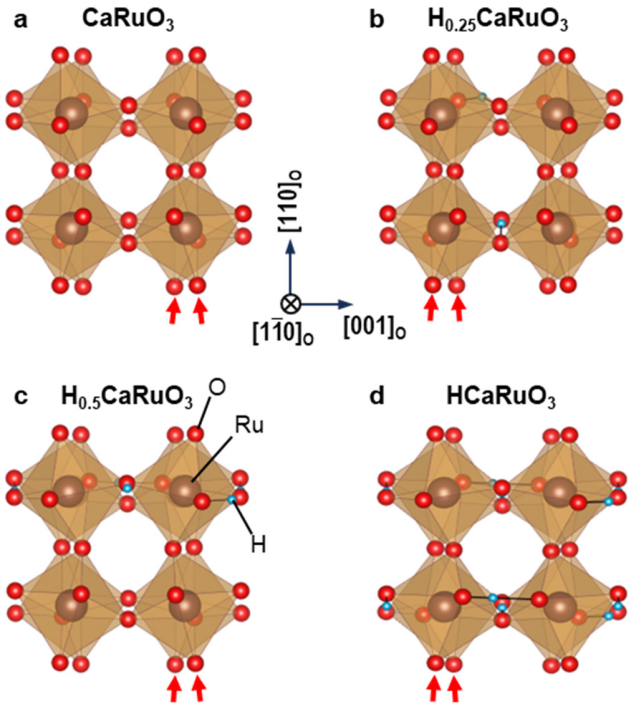

Supplementary Fig. 25 | DFT-simulated CRO unit-cells during ILG-induced protonation.
(**a**) DFT-simulated CRO unit-cell. (**b**-**d**) DFT-simulated H_xCaRuO_3 unit-cells with variable H concentration x = 0.25, 0.5, 1. The A-site Ca cations are hidden for clarity.

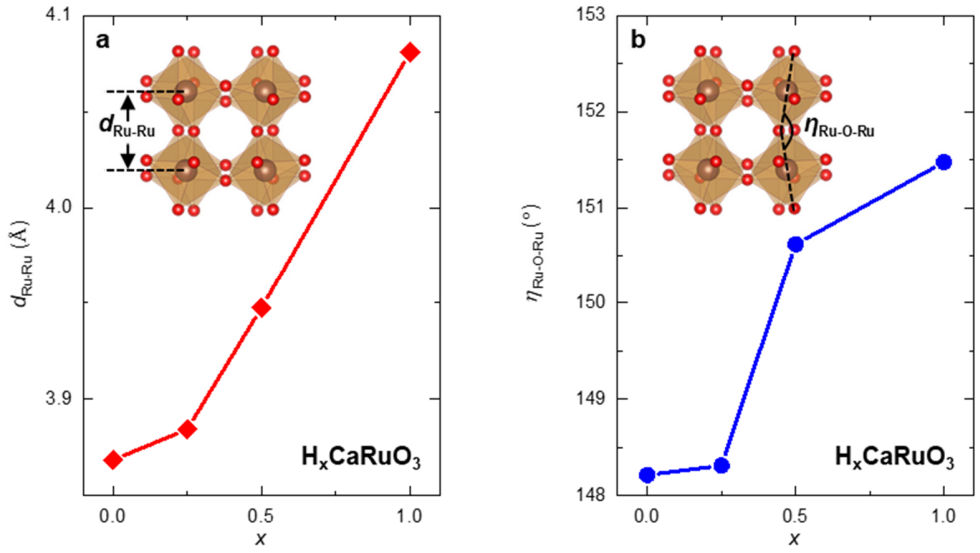

Supplementary Fig. 26 | DFT-calculated structural evolutions of H_xCaRuO_3 unit-cells with variable *x*.

(**a,b**) H concentration *x*-dependent d_{Ru-Ru} (a) and $\eta_{Ru-O-Ru}$ (b) values, extracted from the DFT-calculated H_xCaRuO_3 unit-cells.

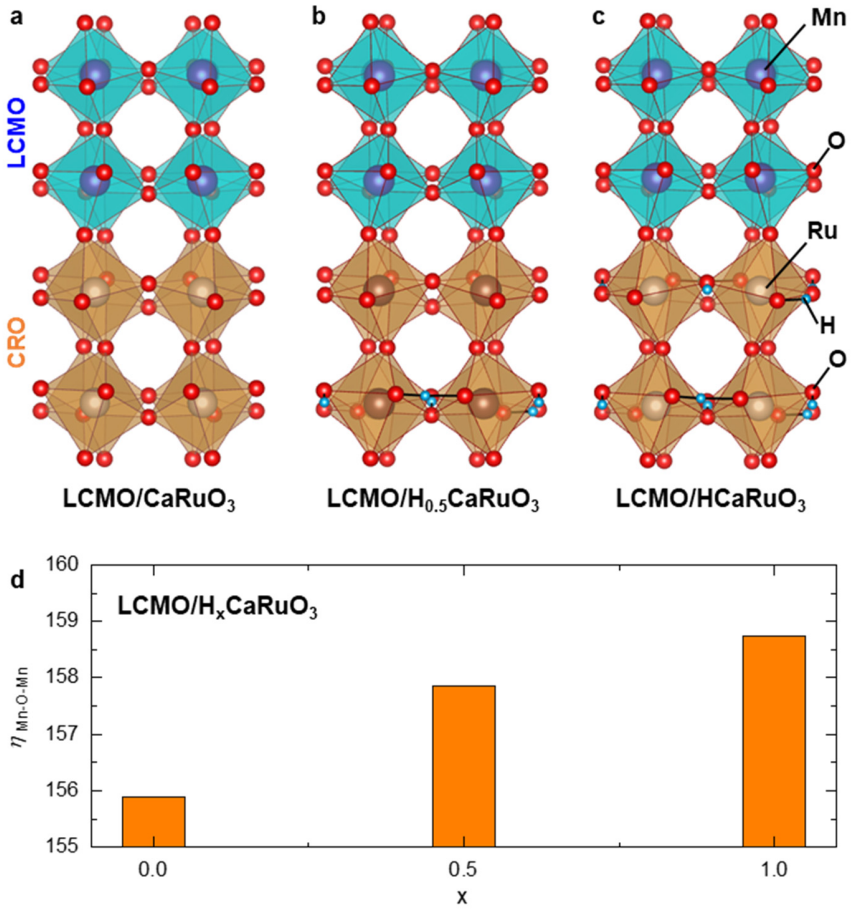

Supplementary Fig. 27 | DFT-calculated structural evolutions of LCMO/H_xCaRuO_3 unit-cells with variable *x*.

(**a-c**) DFT-simulated LCMO/H_xCaRuO_3 bilayer heterostructures with variable H concentration x = 0 (a), 0.5 (b), 1 (c). (**d**) x-dependent out-of-plane Mn-O-Mn bond angle $\eta_{Mn\text{-}O\text{-}Mn}$.

Reference

1 Salamon, M. B. & Jaime, M. The physics of manganites: Structure and transport. *Reviews of modern physics* **73**, 583 (2001).

2 Chen, B. B. *et al.* Contrasting size-scaling behavior of ferromagnetism in $La_{0.67}Ca_{0.33}MnO_3$ films and $La_{0.67}Ca_{0.33}MnO_3/CaRuO_3$ multilayers. *Applied Physics Letters* **104** (2014).

3 Zhong, Z. & Hansmann, P. Band Alignment and Charge Transfer in Complex Oxide Interfaces. *Physical Review X* **7**, 011023 (2017).

4 Chen, P. F. *et al.* High-T_C ferromagnetic order in $CaRuO_3/La_{2/3}Ca_{1/3}MnO_3$ superlattices. *Applied Physics Letters* **103** (2013).

5 Huang, Z. *et al.* Tuning the ground state of $La_{0.67}Ca_{0.33}MnO_3$ films via coherent growth on orthorhombic $NdGaO_3$ substrates with different orientations. *Physical Review B* **86**, 014410 (2012).

6 Zayak, A. T., Huang, X., Neaton, J. B. & Rabe, K. M. Structural, electronic, and magnetic properties of $SrRuO_3$ under epitaxial strain. *Physical Review B* **74**, 094104 (2006).

7 He, J., Borisevich, A., Kalinin, S. V., Pennycook, S. J. & Pantelides, S. T. Control of Octahedral Tilts and Magnetic Properties of Perovskite Oxide Heterostructures by Substrate Symmetry. *Physical Review Letters* **105**, 227203 (2010).

8 Borisevich, A. Y. *et al.* Suppression of Octahedral Tilts and Associated Changes in Electronic Properties at Epitaxial Oxide Heterostructure Interfaces. *Physical Review Letters* **105**, 087204 (2010).

9 Kan, D. *et al.* Tuning magnetic anisotropy by interfacially engineering the oxygen coordination environment in a transition metal oxide. *Nature Materials* **15**, 432-437 (2016).

10 Liao, Z. *et al.* Controlled lateral anisotropy in correlated manganite heterostructures by interface-engineered oxygen octahedral coupling. *Nature Materials* **15**, 425-431 (2016).

11 Marti, W., Fischer, P., Altorfer, F., Scheel, H. & Tadin, M. Crystal structures and phase transitions of orthorhombic and rhombohedral $RGaO_3$ (R= La, Pr, Nd) investigated by neutron powder diffraction. *Journal of Physics: Condensed Matter* **6**, 127 (1994).

12 Vidya, R., Ravindran, P., Kjekshus, A., Fjellvåg, H. & Hauback, B. C. Magnetic properties of Ca-doped $SrRuO_3$ from full-potential calculations. *Journal of Solid State Chemistry* **177**, 146-158 (2004).

13 Guo, Y., Roy, S. & Ali, N. Effect of nitrogen incorporation in $La_{2/3}Ca_{1/3}MnO_3$ manganite. *Journal of Physics: Condensed Matter* **14**, 181 (2001).

14 Hÿtch, M. J. & Minor, A. M. Observing and measuring strain in nanostructures and devices with transmission electron microscopy. *MRS Bulletin* **39**, 138-146 (2014).

15 Hÿtch, M. J., Snoeck, E. & Kilaas, R. Quantitative measurement of displacement and strain fields from HREM micrographs. *Ultramicroscopy* **74**, 131-146 (1998).

16 Lu, N. *et al.* Electric-field control of tri-state phase transformation with a selective dual-ion switch. *Nature* **546**, 124-128 (2017).

17 Liu, Z., Wei, M., Hou, D., Gao, Y. & Niu, Q. Multipolar anisotropy in anomalous Hall effect from spin-group symmetry breaking. *Physical Review X* **15**, 031006 (2025).

18 Ai, W., Chen, F., Liu, Z. et al. Observation of giant room-temperature anisotropic magnetoresistance in the topological insulator β-Ag_2Te. *Nat Commun* **15**, 1259 (2024).

19 Taskin, A.A., Legg, H.F., Yang, F. et al. Planar Hall effect from the surface of topological insulators. *Nat Commun* **8**, 1340 (2017).

20 Tang H X, Kawakami R K, Awschalom D D, et al. Giant planar Hall effect in epitaxial (Ga, Mn) As devices. *Physical review letters* **90**, 107201 (2003).

21 Guan, Y., Han, H., Li, F., Li, G. & Parkin, S. S. P. Ionic Gating for Tuning Electronic and Magnetic Properties. *Annual Review of Materials Research* **53**, 25-51 (2023).

22 Shen, S. *et al.* Emergent Ferromagnetism with Fermi-Liquid Behavior in Proton Intercalated $CaRuO_3$. *Physical Review X* **11**, 021018 (2021).